

# Linear and Rationally Designed Stapled Peptides Abrogate TLR4 Pathway and Relieve Inflammatory Symptoms in Rheumatoid Arthritis Rat Model

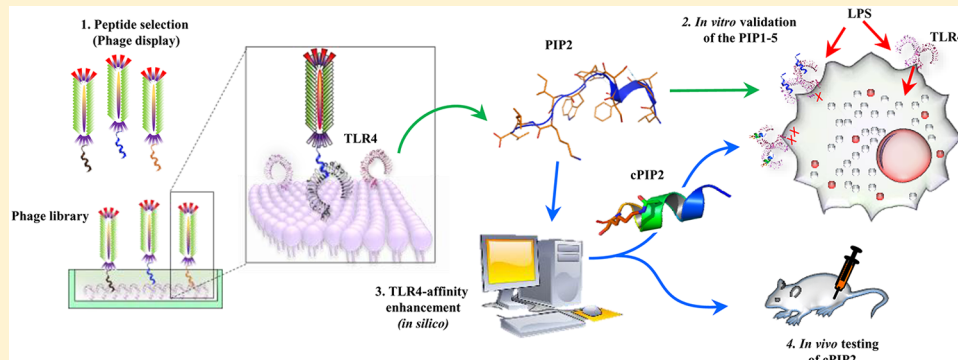
Asma Achek,<sup>†</sup> Masaud Shah,<sup>†</sup> Ji Young Seo,<sup>†</sup> Hyuk-Kwon Kwon,<sup>‡</sup> Xiangai Gui,<sup>†</sup> Hyeon-Jun Shin,<sup>†</sup> Eun-Young Cho,<sup>†</sup> Byeong Sung Lee,<sup>†</sup> Dong-Jin Kim,<sup>§</sup> Sang Ho Lee,<sup>§</sup> Tae Hyeon Yoo,<sup>†</sup><sup>¶</sup> Moon Suk Kim,<sup>†</sup><sup>¶</sup> and Sangdun Choi<sup>\*</sup>,<sup>†</sup><sup>¶</sup>

<sup>†</sup>Department of Molecular Science and Technology, Ajou University, Suwon 16499, Korea

<sup>‡</sup>Department of Orthopedics and Rehabilitation, Yale University School of Medicine, New Haven, Connecticut 06520-8071, United States

<sup>§</sup>Division of Nephrology, Department of Internal Medicine, Kyung Hee University Hospital at Gangdong, Seoul 05278, Korea

## S Supporting Information



**ABSTRACT:** A mounting evidence exists for the despicable role of the aberrant immune response in the pathogenesis of rheumatoid arthritis (RA), where toll-like receptor 4 (TLR4) can activate synovial fibroblasts that lead to the chronic inflammation and joint destruction, thus making TLR4 a potent drug target in RA. We report that novel TLR4-antagonizing peptide, PIP2, inhibits the induction of inflammatory biomarkers in vitro as well as in vivo. Systemically, PIP2 inhibits the lipopolysaccharide (LPS)-elicited TNF- $\alpha$ , IL-6, and IL-12p40 in a mouse model. The rationally designed cyclic derivative, cPIP2, is capable of inhibiting LPS-induced proinflammatory cytokines at significantly lower concentration as compared to PIP2 (PIP2 IC<sub>50</sub> = 20  $\mu$ M, cPIP2 IC<sub>50</sub> = 5  $\mu$ M). Finally, cPIP2 was able to relieve the inflammatory symptoms and synovial tissue destruction in the RA rat model. Cumulatively, these data suggest that PIP2 and cPIP2 hold strong promise for the development of peptide-based immunotherapeutics that could be of great value in curbing TLR-related immune complications including RA.

## INTRODUCTION

Toll-like receptor 4 (TLR4) has been extensively studied owing to its involvement in several immune-related pathologies.<sup>1,2</sup> Unlike other TLRs, TLR4 can induce both myeloid differentiation primary response gene 88 (Myd88)-dependent and the Toll/interleukin-1 receptor (TIR)-domain-containing adapter-inducing interferon- $\beta$  (TRIF)-dependent pathways.<sup>3</sup> The triggering of the MyD88-dependent pathway results in the early phase activation of nuclear factor- $\kappa$ B (NF- $\kappa$ B) and mitogen-activated protein kinases (MAPKs), which leads to the subsequent production of proinflammatory cytokines such as interleukin 6 (IL-6), IL-1 $\beta$ , and tumor necrosis factor  $\alpha$  (TNF- $\alpha$ ). TLR4 stimulation, via the TRIF-dependent pathway, leads to the late phase activation of NF- $\kappa$ B and interferon regulatory transcription factor 3 (IRF3). Both pathways induce

the maturation and activation of innate immune cells such as macrophages and dendritic cells.<sup>4–6</sup>

Although the beneficial effects of TLR4 activation during the host defense response are attributed predominantly to the production of proinflammatory cytokines, aberrant TLR4 signaling causes an inflammatory feedback loop and the onset of an array of acute and chronic human diseases.<sup>7–9</sup> TLR4-targeting therapeutic agents developed so far comprise polysaccharides, glycolipids, antibodies, small molecules, and oligopeptides. These agents have been actively developed, and some are in clinical trials as drugs/adjuvants that can reduce the secretion of proinflammatory cytokines to prevent or

Received: January 10, 2019

Published: June 24, 2019

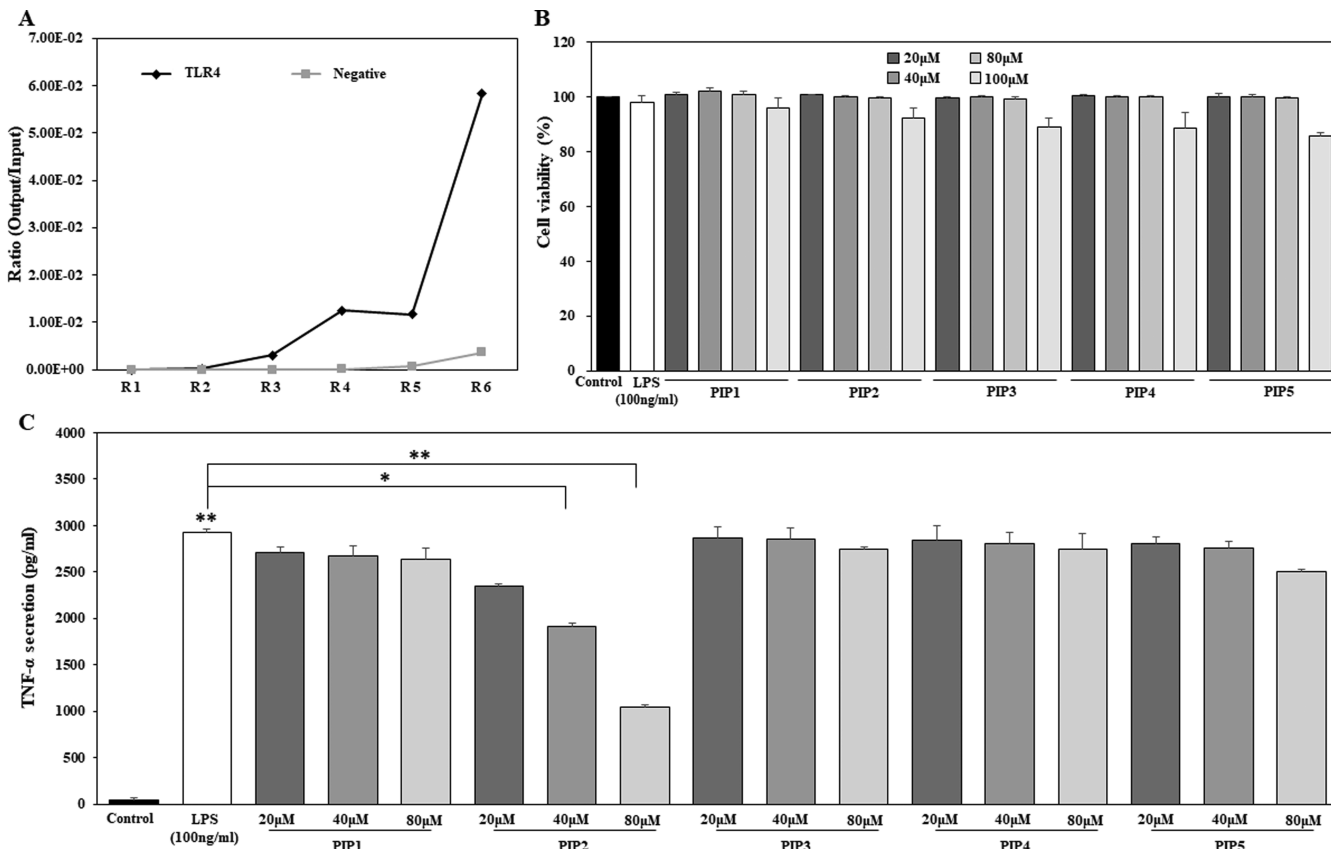


**Figure 1.** Screening of the TLR4-binding peptides. (A) The enrichment of recombinant hTLR4 protein-bound specific phages was evaluated by the output/input ratio of the collected phages after each round of panning. (B) RAW264.7 cells were treated with various concentrations of PIPs for 24 h, and cell viability was measured using the MTT assay. (C) The TNF- $\alpha$  secretion was assessed by ELISA in RAW264.7 cells with different concentrations of PIPs. All experiments were performed in duplicate and were conducted independently ( $n = 3$ ). The mean  $\pm$  SEM values of the independent experiments were calculated and used in the two-tailed paired Student's  $t$ -test (\* $P < 0.05$ , \*\* $P < 0.01$ ).

relieve inflammatory diseases.<sup>10,11</sup> TAK-242 (resatorvid),<sup>12</sup> which binds to the intracellular TIR domain of TLR4, and eritoran (E5564),<sup>13</sup> binding to the lipopolysaccharide (LPS)-binding pocket on MD2, are reported to block the downstream signaling cascade. Also, FP7, a diphosphorylated diacylated monosaccharide, selectively repressed the TLR4-dependent signaling by directly competing with LPS for MD2 binding.<sup>14</sup> Furthermore, Cighetti et al.<sup>15</sup> reported a synthesized monosaccharide lipid A-mimetic that inhibits the LPS-induced TLR4 signaling through its binding to MD2. Advances in natural and synthetic TLR4 modulators have been previously discussed and reviewed thoroughly by numerous studies.<sup>16–19</sup> Moreover, *Mycobacterium w* was shown to exert an antagonistic effect on TLR4 and is currently in a phase III clinical trial for its efficacy in patients with severe sepsis (NCT02330432). Antibodies have also been developed for the treatment of autoimmune and inflammatory diseases. NI-0101 (also known as 15C1, sponsored by Novimmune) is a monoclonal antibody that blocks TLR4 signaling and successfully prevents cytokine release following a systemic LPS challenge.<sup>20</sup> The phase I clinical trials of NI-0101 have been completed, presenting good safety, tolerability, and elimination profiles (NCT01808469 and NCT03241108).

Overall, various approaches have been utilized for the development of new drugs with the ability to downmodulate the TLR4-mediated inflammation. One strategy used in drug discovery is phage display (PD) technology. PD is one of the most powerful research tools employed in various protein

interaction studies to identify new peptides from a random phage library screened against specific target proteins.<sup>21</sup> As this method represents an effective approach for the identification of binders with high affinity, it was employed in the present study to identify novel peptides that could abrogate the TLR4 pathway. Our empirical results confirmed that phage-display-derived inhibitory peptide 2 (PIP2) has the potential to block the in vitro LPS-induced TLR4 signaling. The in silico protein design strategy was utilized to enhance the stability and efficacy of PIP2 through the manipulation of the structural information of the TLR4–PIP2 complex. Moreover, peptide cyclization has been widely implemented to enhance the half-life of the peptide drugs and also increase their cellular uptake.<sup>22,23</sup> Cyclic PIP2 (cPIP2), cyclized through a lactam bridge, was tested for its structural stability and biological activity, both in silico and in vitro, displaying a relatively stable protein dynamics and an enhanced inhibitory effect on the LPS-induced TLR4 signaling pathway.

## RESULTS

**Screening of a Phage-Displayed Peptide Library against TLR4.** The pHEN2 (12-mer) PD library was constructed and exposed to a 96-well plate coated with the recombinant human TLR4 (hTLR4) protein, as previously described.<sup>24</sup> Six rounds of biopanning were conducted to enrich the PD library against hTLR4. After each round, the enrichment ratio was evaluated through the titer of the eluted phages (Figure 1A). The phage clones capable of binding

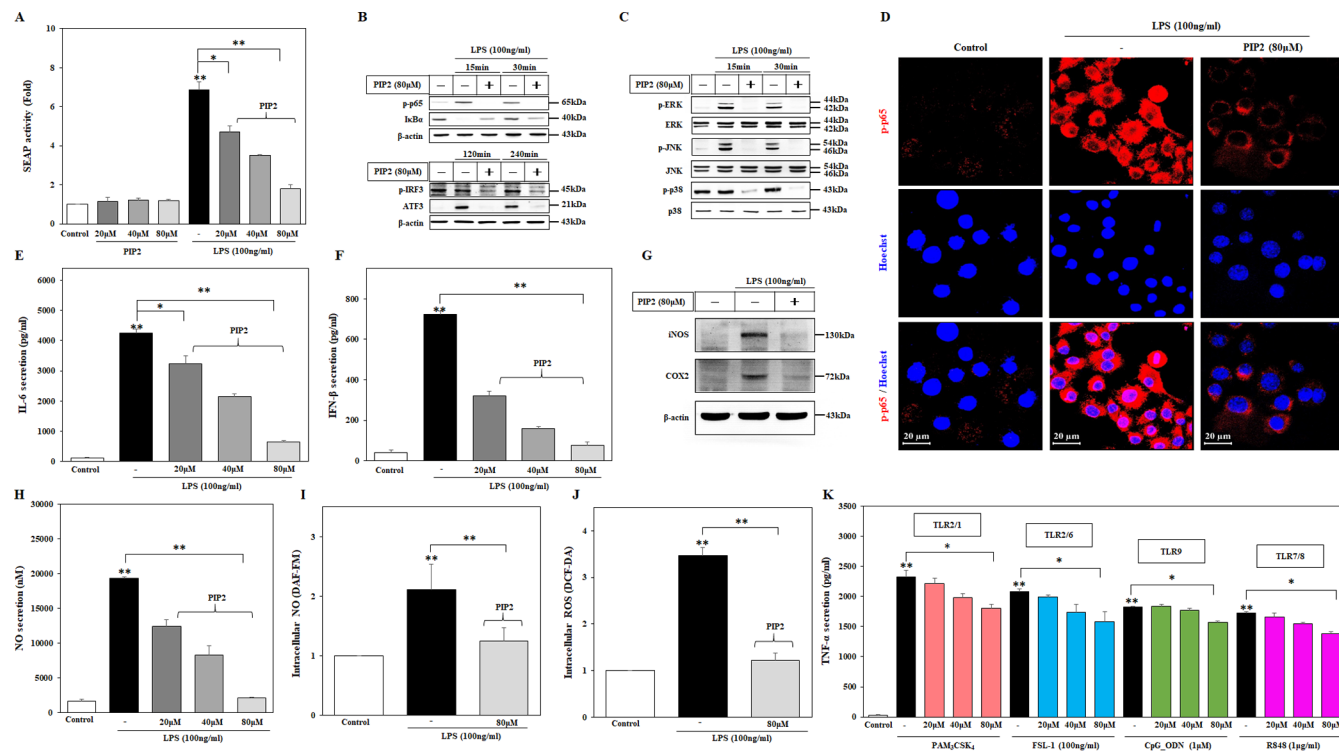


**Figure 2.** Inhibitory effect of PIP2 on the TLR signaling pathway. (A) The inhibitory effect of PIP2 was initially evaluated by monitoring the activation level of NF-κB through the SEAP assay in HEK-Blue hTLR4 cells. (B) The expression level of NF-κB ( $\text{I}\kappa\text{B}\alpha$  cytosolic degradation) was measured by western blotting using whole protein extract from RAW264.7 cells using  $\beta$ -actin as a loading control. The expression levels of p-IRF3 and ATF3 were also measured by western blotting using whole protein extracts. (C) The expression levels of the MAPKs, including p-ERK, p-JNK, and p-p38, were measured in whole protein extracts of PIP2-treated cells for 15 or 30 min. The inactive MAPKs, ERK, JNK, and p38 were used as controls. (D) The expression level of p-p65 was measured by immunofluorescence staining and detected by confocal microscopy. The red staining indicates the phosphorylated NF-κB (p-p65), and the blue staining, Hoechst, corresponds to the nucleus staining (scale bar = 20  $\mu\text{m}$ ). (E, F) The secretion levels of IL-6 and IFN- $\beta$  were measured in RAW264.7 cells by ELISA. (G) The expression levels of iNOS and COX2 were measured in RAW264.7 cells by western blotting.  $\beta$ -Actin was used as a loading control. (H) The production of NO was evaluated using the NO secretion kit. (I) The cytosolic secretion level of NO was measured by fluorescence-activated cell sorting (FACS) with DAF-DA staining, and (J) the generation of ROS was measured in the cytosol by FACS using DCF-DA staining. (K) The comparative secretion level of TNF- $\alpha$  was evaluated in PIP2-treated RAW264.7 cells under the influence of different TLR ligands [TLR2/1 (PAM<sub>3</sub>CSK<sub>4</sub>), TLR2/6 (FSL-1), TLR9 (CpG-ODN), or TLR7/8 (RS48)]. All data shown represent the results of three independently conducted experiments ( $n = 3$ ) performed in duplicate; the mean  $\pm$  SEM of the independent experiments was calculated and used in the two-tailed paired Student's *t*-test (\* $P < 0.05$ , \*\* $P < 0.01$ ).

hTLR4 were selected by phage-enzyme link immunosorbent assay (phage-ELISA) and sequenced to estimate their nucleotide variation by using BioEdit software.<sup>25</sup> The two peptides, PIP1 and PIP4, were identical except for two residues in their N-terminals; however, other peptides were unique and contained predominantly hydrophobic residues. Five 12-mer peptides, designated as PIP1–PIP5, having unique sequences (Supporting Table 1), were synthesized and tested for their cytotoxicity in RAW264.7 cells by using a concentration gradient between 20 and 100  $\mu\text{M}$ . At concentrations below 80  $\mu\text{M}$ , none of the peptides were cytotoxic; however, the viability of cells treated with 100  $\mu\text{M}$  peptides was slightly reduced (Figure 1B). Therefore, further experiments were conducted using concentrations between 20 and 80  $\mu\text{M}$ . The preliminary investigation suggested that among the selected PIPs, PIP2 significantly diminished the TNF- $\alpha$  secretion in a dose-dependent manner (Figure 1C). This was confirmed through ELISA in RAW264.7 cells treated with PIPs in the presence of LPS. The physiochemical properties of PIP2 were further investigated to estimate its TLR4-specific tendency, and subsequent experiments were conducted to standardize the antagonistic effect of PIP2 on TLR4 signaling.

### PIP2 Inhibits the TLR4 Signaling Pathway in RAW264.7 Cells.

The secreted embryonic alkaline phosphatase (SEAP) reporter gene is under the control of the IL-12p40 minimal promoter, which contains the NF-κB- and activator protein 1 (AP-1)-binding sites, and is induced upon TLR4 activation.<sup>26</sup> Hence, the TLR4-inhibitory activity was measured by the SEAP assay using different concentrations of PIP2 (20, 40, or 80  $\mu\text{M}$ ) with respect to LPS. As expected, LPS-treated cells showed an induced activation of NF-κB, whereas the cells pretreated with PIP2 for 1 h and then co-stimulated with LPS for 24 h showed a significant dose-dependent decrease in SEAP activity (Figure 2A). Conversely, SEAP activity was unaffected in cells treated with only PIP2. Furthermore, the inhibitory effect of PIP2 was investigated in LPS-stimulated RAW264.7 cells to monitor the activation of NF-κB and MAPKs through western blotting. PIP2 significantly suppressed the LPS-induced activation of NF-κB and  $\text{I}\kappa\text{B}\alpha$  degradation (Figure 2B). In addition, PIP2 also inhibited the activation of the activating transcription factor 3 (ATF3) and the phosphorylation of IRF3. Further, western blot data suggested that PIP2 successfully hindered the activation of MAPKs, including the phosphorylation of ERK, JNK, and p38, compared with the activation levels in LPS-treated cells

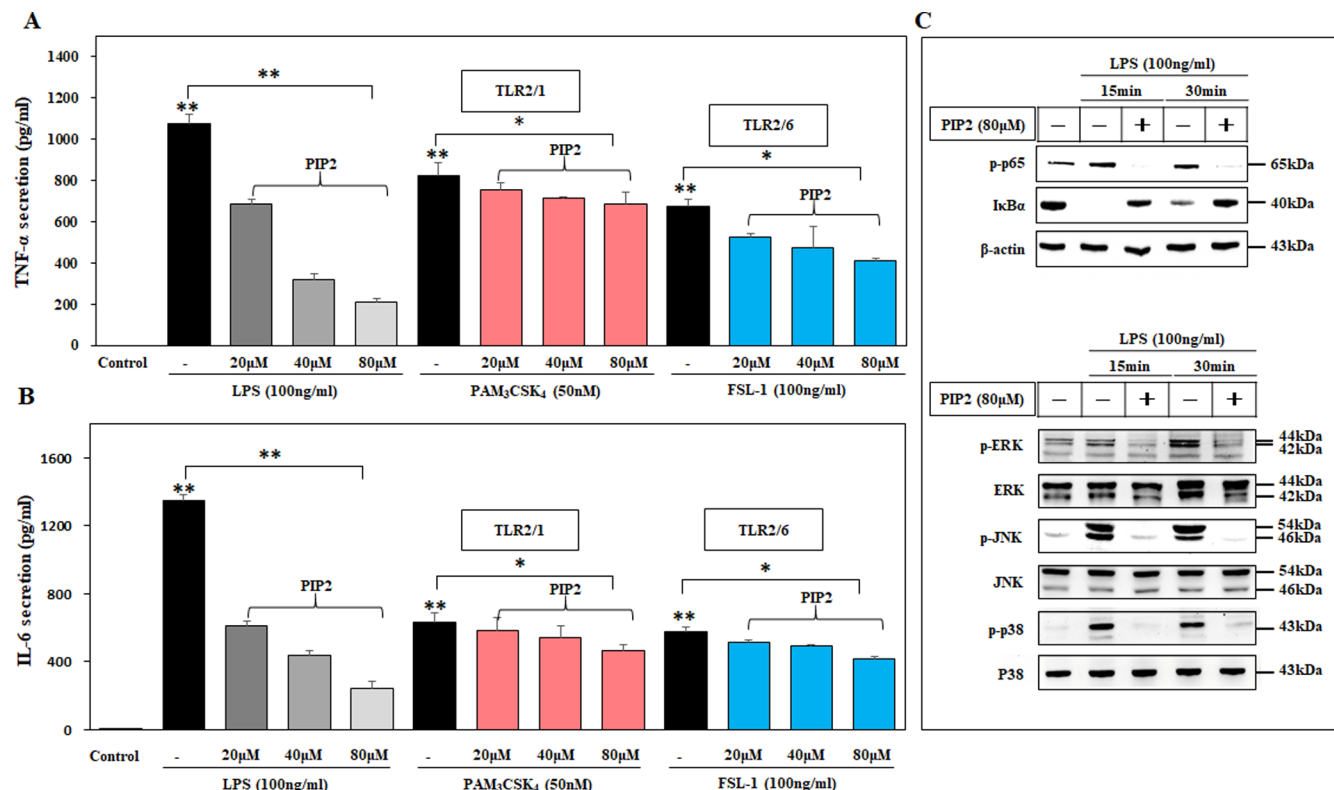


**Figure 3.** PIP2 inhibits cytokine secretion, and NF-κB and MAPKs activation in human peripheral blood mononuclear cells (hPBMCs). The secretion level of (A) TNF- $\alpha$  and (B) IL-6 was evaluated in PIP2-treated hPBMCs under the influence of TLR4 ligand LPS, TLR2/1 ligand PAM<sub>3</sub>CSK<sub>4</sub>, and TLR2/6 ligand FSL-1. (C) NF-κB activation and the degradation of IκB $\alpha$ , as well as the expression level of MAPKs, were evaluated by western blotting using the whole protein extract. The inactive MAPKs were used as controls, and β-actin was used as a loading control. All data shown are the results of independently conducted experiments ( $n = 4$ ) performed in duplicate, and the mean  $\pm$  SEM values of the independent experiments were calculated and used in the two-tailed paired Student's *t*-test (\* $P < 0.05$ , \*\* $P < 0.01$ ).

(Figure 2C). Confocal microscopy also confirmed the inhibitory effect of PIP2 via the alleviation of the LPS-induced p-p65 expression level (Figure 2D). Eventually, the LPS-induced production of IL-6 and IFN- $\beta$  was also significantly hindered by PIP2 in a dose-dependent manner (Figure 2E,F). The generation of ROS and NO is directly related to the cellular level of iNOS and other factors.<sup>27–30</sup> Hence, iNOS and COX2 levels were monitored in LPS-stimulated cells that were pretreated with PIP2. PIP2 effectively repressed LPS-induced iNOS and COX2 expression (Figure 2G).

Similarly, the intracellular generation of NO and ROS, as well as the extracellular secretion of NO, was inhibited by PIP2 (Figure 2H–J). To ascertain the effect of PIP2 on other TLRs and their downstream signaling, the cells were treated with PIP2 together with PAM<sub>3</sub>CSK<sub>4</sub> (for TLR1/2), FSL-1 (for TLR2/6), resiquimod/R848 (for TLR7/8), or CpG-ODN (for TLR9). Subsequently, the secretion level of TNF- $\alpha$  was monitored by ELISA, which suggested that PIP2 nonsignificantly inhibited TLR2/1- and 2/6- and, to a lesser extent, TLR7/8- and 9-mediated TNF- $\alpha$  secretion (Figure 2K).

These data indicate that, owing to the structural and sequence similarity of the TLR ectodomains (ECDs), PIP2 might have low-affinity binding sites on TLR1/2/6 and nonspecifically alter their downstream signaling. This was partly supported by the surface plasmon resonance (SPR) results (Supporting Figure 1). Collectively, these findings suggested that PIP2 significantly stalled both arms of the TLR4

pathway (the MyD88-dependent and TRIF-independent pathways) in LPS-induced RAW264.7 cells.

**PIP2 Abrogates TLR Signaling in Human Peripheral Blood Mononuclear Cells (hPBMCs).** The immune inhibitory effect of PIP2 was evaluated in hPBMCs through the estimation of the cytokine secretion and protein expression through western blotting. The secretion of TNF- $\alpha$  and IL-6 was investigated by ELISA in cells treated with various concentrations of PIP2 in the presence of LPS, PAM<sub>3</sub>CSK<sub>4</sub>, or FSL-1. PIP2 significantly inhibited the LPS-mediated secretion of TNF- $\alpha$  and slightly hindered its secretion in PAM<sub>3</sub>CSK<sub>4</sub> or FSL-1-stimulated cells (Figure 3A). Similarly, the LPS-induced secretion of IL-6 was considerably suppressed after co-treatment with PIP2, but this effect was marginal in PAM<sub>3</sub>CSK<sub>4</sub> or FSL-1-stimulated cells (Figure 3B). The LPS-mediated activation of MAPKs was also evaluated in hPBMCs. PIP2-treated cells showed considerably reduced phosphorylation of NF-κB and suppressed degradation of IκB $\alpha$  (Figure 3C). In addition, the expression level of MAPKs, including p-ERK, p-JNK, and p-p38, was significantly inhibited in PIP2-treated cells.

**PIP2 Suppresses TLR4-Mediated Inflammatory Response in Mice Bone-Marrow-Derived Macrophages (mBMDMs) and LPS-Induced Systemic Cytokine Response in Vivo.** Similar to RAW264.7 cells and hPBMCs, the TLR inhibitory effect of PIP2 was further evaluated in mBMDMs through the assessment of the LPS-induced secretion of TNF- $\alpha$ , IL-6, and IFN- $\beta$ . PIP2 significantly inhibited the secretion of proinflammatory cytokines and IFN-

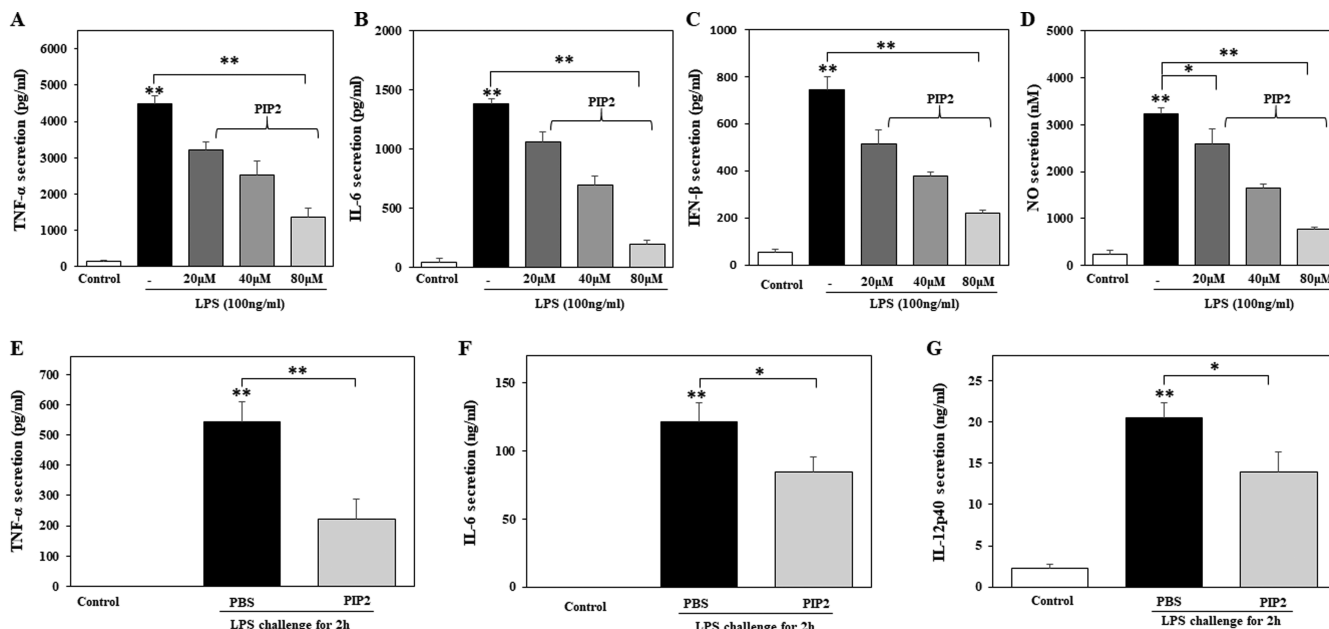


**Figure 4.** PIP2 hinders TLR4-mediated cytokine secretion in mice bone-marrow-derived macrophage (mBMDM) and alleviates TLR4-mediated inflammatory response in vivo. The secretion levels of (A) TNF- $\alpha$ , (B) IL-6, and (C) IFN- $\beta$  were assessed in PIP2-treated mBMDMs and found to be significantly reduced. (D) NO secretion was evaluated in the same cells by using the NO secretion kit. (E–G) C57BL/6J mice were intraperitoneally (i.p.) treated with PBS (control) or with 70 nmol/g PIP2 for 1 h followed by i.p. administration of LPS (5  $\mu$ g/g). Plasma samples were obtained from five mice in each group (control and PIP2-treated), and the levels of systemic cytokines (E) TNF- $\alpha$ , (F) IL-6, and (G) IL-12p40 were monitored. All data shown are the result of independent experiments ( $n = 4$ ) performed in duplicate. The mean  $\pm$  SEM values of the independent experiments were calculated and used in the two-tailed paired Student's *t*-test (\* $P < 0.05$ , \*\* $P < 0.01$ ).

$\beta$  in these cells (Figure 4A–C). Moreover, PIP2 also inhibited LPS-elicited NO secretion in mBMDMs in a dose-dependent manner (Figure 4D). Subsequently, the immune inhibitory effect of PIP2 was evaluated in vivo through the measurement of the level of systemic cytokines in mice. C57BL/6J mice were pretreated intraperitoneally (i.p.) with PIP2 and challenged for 2 h with LPS (5  $\mu$ g/g of mouse weight). The mice were injected with the peptides at a dose of 70 nmol/g of mouse weight 1 h before LPS stimulation. IL-6, TNF- $\alpha$ , and IL-12p40 were measured in the plasma samples collected before and 2 h after challenge. We found that PIP2 treatment decreased the LPS-induced systemic secretion of these cytokines in a significant manner (Figure 4E–G).

**Structural Investigations of PIP2 and Plausible TLR4 Inhibitory Mechanism.** To confirm the binding of PIP2 to TLR4, fluorescein isothiocyanate (FITC) was conjugated to the N-terminus of the peptide. RAW264.7 cells were treated with FITC-PIP2 for 1 h before LPS treatment, and the fluorescence intensities of FITC-PIP2 and TLR4 were measured using immunofluorescence staining and confocal microscopy. The localization of TLR4 and FITC-PIP2 was monitored with respect to the position of the nucleus. TLR4 was localized on the plasma membrane in the LPS-treated cells. Remarkably, FITC-PIP2 was also localized on the plasma membrane and its signal almost coincided with TLR4 fluorescence. The treatment of cells with both FITC-PIP2 and LPS confirmed that FITC-PIP2 and TLR4 overlapped perfectly on the plasma membrane, providing a yellow signal (Figure 5A). Furthermore, we studied the binding affinity of PIP2 to TLR4 and MD2 through SPR, a method that allows the study of the biophysical interaction of macromolecules, nucleic acids, and small molecules.<sup>31</sup> Recombinant hTLR4 protein and recombinant hMD2 protein (used ligands) were

immobilized on the SPR sensor chip. PIP2 (analyte) was added to the sensor chip at different concentrations between 12.5 and 200  $\mu$ M. The calculated association ( $k_a$ ) and dissociation ( $k_d$ ) values were recorded as  $3.45 \times 10^4$  M $^{-1}$  S $^{-1}$  and  $1.13 \times 10^{-2}$  S $^{-1}$  for PIP2-TLR4 and  $1.27$  M $^{-1}$  S $^{-1}$  and  $4.92 \times 10^{-4}$  S $^{-1}$  for PIP2-MD2, respectively. Nonetheless, PIP2 exhibited a dose-dependent binding to MD2 at lower concentration (<50  $\mu$ M) as compared to TLR4 (Figure 5B). MD2 contains a single cavity to accommodate the binding ligand, and PIP2 has a flexible nature; this flexibility and structural freedom could be a possible factor that hinders the binding of PIP2 with MD2 at higher concentration.

Similar conditions were used for the PIP2 and TLR2 binding kinetics. Nonetheless, we observed a concentration-independent interaction pattern between PIP2 and TLR2, as presented in Supporting Figure 1. PIP2 was used as an analyte at concentrations of 12.5, 25, and 50  $\mu$ M, which corresponded to a narrow window of response units (RU), 8–9. This was further supported by the overlapping RU values when 100 and 200  $\mu$ M PIP2 concentrations were used. These and the nonsignificant in vitro results, discussed above, could partly explain that the interaction of PIP2 with TLR2 is nonspecific.

Once confirmed through cell imaging and SPR analysis, the potential interaction of PIP2 with TLR4 was further investigated through in silico analysis. PIP2 oligopeptide was modeled through computational procedures, which were used to predict its binding configuration with TLR4 that was confirmed to be modulated in PIP2-treated in vitro systems. The secondary structure predicted by I-TASSER<sup>32</sup> and PSIPRED suggested that the N- and C-termini of the peptide were coiled, while the central part was predominantly helical (Supporting Table 1). The 3D structures suggested by I-TASSER<sup>32</sup> and those built by MOE did not show any strands

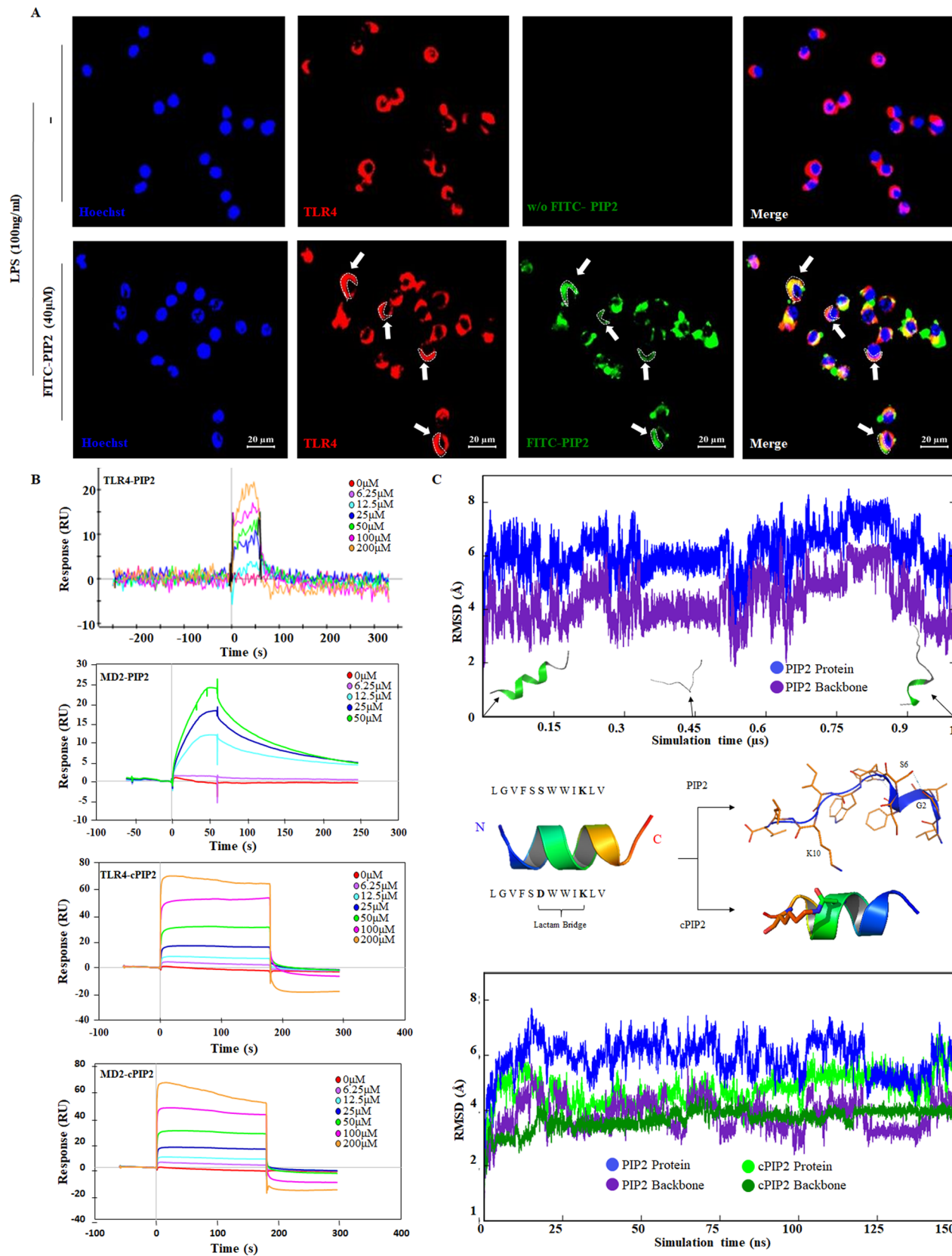


**Figure 5.** Imaging and biophysical analysis of the PIP2-TLR4 complex and structural evaluation of PIP2. (A) The expression level of TLR4 (red staining) and the localization of FITC-PIP2 (green staining) were evaluated by immunofluorescence and detected using confocal microscopy. Hoechst staining (blue color) corresponds to the nuclei (scale bar = 20  $\mu$ m). The confocal images show co-localization of the FITC-PIP2 and TLR4. (B) The binding affinities of PIP2 and cPIP2 were evaluated using SPR. The hTLR4 and hMD2 were immobilized to the sensor chip, and the peptides were used as analyte. The sensorgram suggests that PIP2 and cPIP2 bind to TLR4 ECD and MD2 in a concentration-dependent manner. (C) Molecular dynamics simulation (MDS) was performed for PIP2. The N-terminus of PIP2 retains its helical structure at the end of

Figure 5. continued

MDS; however, the C-terminus half acquired a loop structure. The root-mean-square deviation (RMSD) of the whole protein (blue) and backbone atoms (purple) to its initial conformation during MDS is presented using the least-square fit. The helical structure of PIP2 is stabilized through the establishment of a lactam bridge between Asp6 and Lys10 (cPIP2). Comparative MDS suggested that the lactam bridge significantly stabilized the structure of PIP2 (green and fluorescent green RMSD plots represent the backbone and whole protein RMSD, respectively). Color codes are provided for further details.

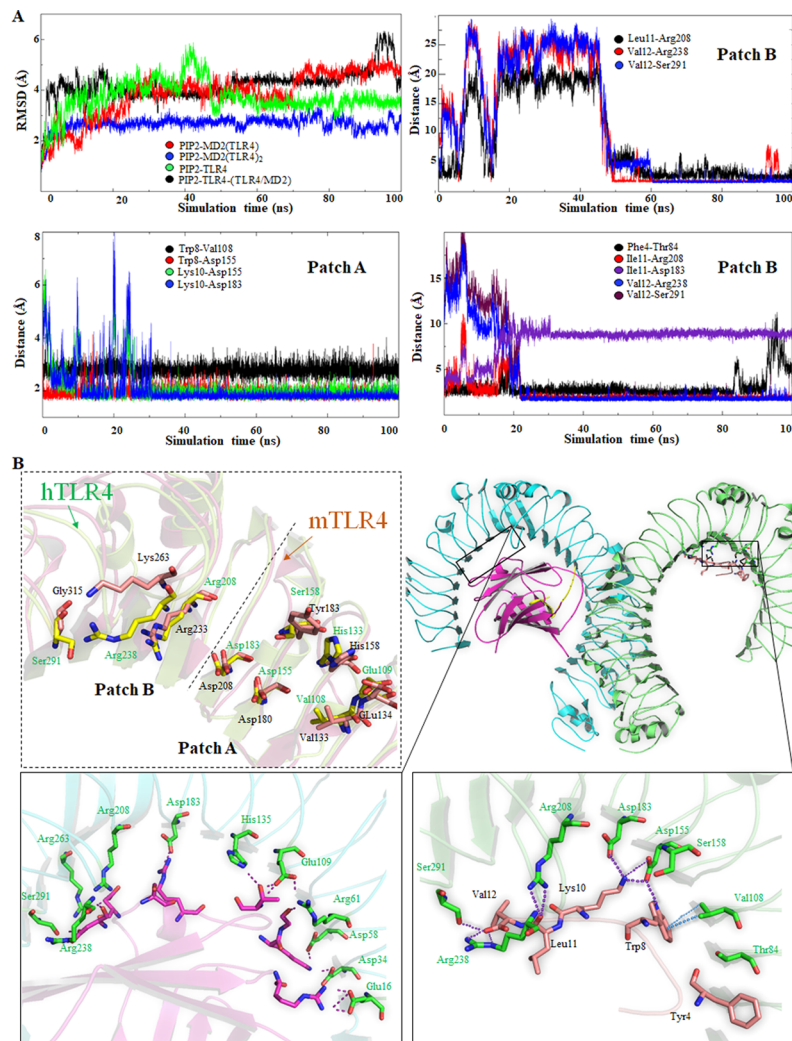


**Figure 6.** Structural dynamics of TLR4-bound PIP2 and comparative interfacial analysis of TLR4/MD2 and PIP2-TLR4. (A) The root-mean-square deviation (RMSD) of the backbone atoms and whole PIP2 peptide, bound to either TLR4 or MD2, was calculated using the least-square fit. Hydrogen-bond distances are calculated as a function of time between the interaction of the residues of PIP2 and the patch A and B residues of the ECD of TLR4. The top-right panel in 'A' indicates the time-dependent establishment of hydrogen-bond interaction between PIP2 and patch B of the monomeric TLR4 (first simulation). The lower two panels validate the initial simulation and suggest that PIP2 established strong electrostatic interactions with patch A and patch B of TLR4 when docked-simulated with the PIP2-TLR4 (TLR4/MD2) complex (second simulation). (B) Cartoon representations that explain the amino acid identity/similarity between human and mouse TLR4, which interact with MD2 and PIP2. These illustrations suggestively confer that PIP2 competitively interacted with the MD2-binding patches A and B of TLR4, thereby blocking LPS-induced TLR4 activation. Note: TLR4 amino acid numbering has been renumbered according to the model used. The PDB coordinates of TLR4 and MD2 were downloaded from the PDB database (PDB ID: 3FXI).

and primarily exhibited a helical topology (Figure 5C). To normalize and stabilize the predicted structure of PIP2, we utilized a well-established molecular dynamics simulation (MDS) system. Physiological saline conditions were provided to the peptide, and a 1  $\mu$ s MDS was conducted. The 3D coordinates were sampled and have been provided as Supporting Movie part 1. This suggested that the N-terminus of PIP2 retained its helical structure and the C-terminus transformed into a wipe-like looped structure. The helical

topology is retained by the electrostatic interaction between the polar sidechain of Ser6 and the backbone oxygen of Val3 (Figure 5C).

Stapling small peptides to enhance their half-life and retain their secondary structures has been widely utilized.<sup>33–35</sup> Considering the flexible C-terminus of PIP2 and assuming that this could reduce the TLR4 inhibition efficacy, we implemented the peptide stapling strategy to enhance the stability of PIP2. After conducting a number of possible

changes (discussed in [Experimental Section](#)), the polar Ser6 was substituted with aspartic acid, and a lactam bridge was established between Asp6 and Lys10. To scale the effect of stapling on the overall structure of cPIP2, the cyclic form of PIP2, the molecular dynamics (MD) trajectory was visualized in an animated movie and compared with that of PIP2. We observed that PIP2 lost its C-terminal helix, although cPIP2 retains a helical conformation throughout the simulation time ([Supporting Movie](#) parts 1 and 2). These results suggested that owing to the stable nature of cPIP2, it could potentially inhibit TLR4 signaling at lower concentrations and longer times as compared with PIP2.

To evaluate that cPIP2 could have durable TLR4-inhibitory effect, the binding affinity of cPIP2 to TLR4 and MD2 was examined through SPR. The calculated  $K_a$  and  $K_d$  constants for the cPIP2–TLR4 interaction were recorded as  $7.32 \times 10^4 \text{ M}^{-1} \text{ S}^{-1}$  and  $1.4 \times 10^{-3} \text{ S}^{-1}$ , respectively. However, for cPIP2-MD2, these values were  $1.04 \times 10^5 \text{ M}^{-1} \text{ S}^{-1}$  and  $2.39 \times 10^{-3} \text{ S}^{-1}$ , respectively. These data suggest that cPIP2 exhibits stronger association and reduced dissociation behaviors with TLR4 and MD2 as compared to PIP2 ([Figure 5B](#)).

**Docking Simulation and Interfacial Analysis of PIP2-Bound TLR4 Complexes.** Our *in vitro* findings suggested that PIP2 significantly halted LPS-induced TLR4 activation. Consequently, we attempted to decipher the possible binding pattern and TLR4-antagonizing effect of PIP2. As discussed, PIP2 was selected through phage-ELISA using a recombinant ECD of human TLR4. Accordingly, PIP2 was docked with the three different states of TLR4 (discussed in [Experimental Section](#)) to locate its preferential binding position. The hydrophobic nature of PIP2 suggests a high probability for nonpolar contacts with its interacting proteins; however, charged lysine in this peptide could establish salt bridges with negatively charged solvent-exposed residues.

When docked with TLR4 alone in a monomeric form, PIP2 displayed an inconsistent binding behavior with its ECD. Among the four docked clusters that PIP2 formed with the TLR4 ECD, only one cluster at the N-terminus was slightly consistent and nondispersed. Approximately 43% of the docked PIP2 was clustered in this particular location of the TLR4. The second cluster, which was very important with respect to the MD2-dependent TLR4 activation, was occupied by ~9% of the docked PIP2. We constructed an interaction database of the top 150 docked poses of PIP2-TLR4 and summarized the contacts through protein ligand interaction fingerprints (PLIF) in [Supporting Figure 2A](#). As expected, most of the interacting residues were nonpolar or hydrophobic. Furthermore, PLIF analysis supported the predominant clustering of PIP2 at the N-terminus of the TLR4 ECD.

To further understand the preferential binding affinity of PIP2 between TLR4 and TLR4/MD2 heterodimer, we docked PIP2 with TLR4/MD2 dimeric and trimeric (one of the bound MD2 was removed, and the second was left bound in the TLR4/MD2 tetramer) complexes. Our data showed that almost all of the docked PIP2 occupied the hydrophobic cavity of the MD2 and did not show any considerable nonspecific clustering with the TLR4 ECD. Next, PLIF analysis was performed for the top 150 PIP2-MD2(TLR4) docked complexes and the consistently interacting key residues were investigated. We observed that the gating loop (Ser120-Lys128) of MD2, which was reported to be involved in the activation of TLR4,<sup>36</sup> was particularly involved in the PIP2 interaction. Ile52 and Phe121 in the gating loop were reported

to interact with more than 80% of the docked PIP2 ([Supporting Figure 2B](#)). However, the key residues of PIP2 involved in this interaction were broadly similar to those observed in PIP2-TLR4 docking.

From these preliminary docking results, we predicted that PIP2 inhibited TLR4 signaling through either binding with the MD2 cavity or competitively hindering MD2 binding with TLR4 (cluster 2). However, the binding of PIP2 in cluster 1 is the least plausible way to block TLR4 signaling. In addition, inhibition of the N-terminus of TLR4 was not reported to abrogate its downstream signaling. Given that these two possible binding poses may inhibit TLR4 signaling, the models were further vetted for structural dynamics using MDS.

**Structural Dynamics of PIP2-Bound TLR4.** Due to the probability that PIP2 could hamper TLR4 signaling by binding with the cavity of MD2 or competitively hindering TLR4 and MD2 interaction, a vital component of TLR4 signaling, two PIP2-docked complexes were initially simulated for 100 ns. First, the stability of TLR4-PIP2 (where PIP2 binds to the central part of TLR4) was examined. Structural dynamics suggested that the docking program placed PIP2 at an appropriate position; however, structural flexibility and limited motions provided by MDS suggested that the backbone oxygen of C-terminus Val and Leu in PIP2 established strong hydrogen bonds with the positively charged Arg208 and 238 and polar Ser291 of TLR4. This was further confirmed by tracking the minimum distances between these residues along the MD trajectory ([Figure 6A](#)). Similar sites in TLR4 were confirmed to be crucial for MD2 binding and denoted patch A and patch B.<sup>36</sup> RMSD plots also indicated that, initially, the backbone atoms of PIP2 vigorously fluctuated and stabilized after the establishment of hydrogen bond contacts at 50 ns of the MD trajectory. An animated movie of PIP2-TLR4, based on 500 frames extracted from the MD trajectory, has been provided in [Supporting Movie](#) part 3.

The detailed analysis of the PIP2-MD2(TLR4) MD trajectory indicated a continuous rise in the RMSD ([Figure 6A](#)). Visual inspection indicated that this deviation resulted from the translational motion of MD2, also influencing the relative stability of PIP2, rather than PIP2-induced conformational changes in the TLR4/MD2 complex. These motions have been captured in a 3D movie and provided in the [Supporting Movie](#) parts 4 and 5. The outward movement of the MD2 was attributable to the fact that we did not consider the influence of adjacent TLR4 on this complex, which also interacted with MD2 and stabilized the whole tetramer during signaling.

To address this discrepancy and validate the binding affinity of PIP2 at patches A and B of TLR4, a single complex containing two TLR4 molecules, one MD2 and two PIP2 molecules was assembled and subjected to MDS. In this case, one of the PIP2 peptides was bound to MD2 and the other, near patches A and B of adjacent TLR4, was not bound to MD2 ([Figure 6B](#)). Interestingly, our analysis showed that the second TLR4 significantly impacted the stability of MD2-bound PIP2 as no outward translational movement of MD2 was observed ([Supporting Movie](#) part 6). However, we did not observe any switch of Phe126 from its active to inactive conformation. Phe126, located in the gating loop of MD2, was previously reported to be crucial for the ligand-dependent TLR4 signaling.<sup>37</sup>

To assess the binding affinity of PIP2 with the MD2-binding patches of TLR4, the PIP2-TLR4 interface in the PIP2-

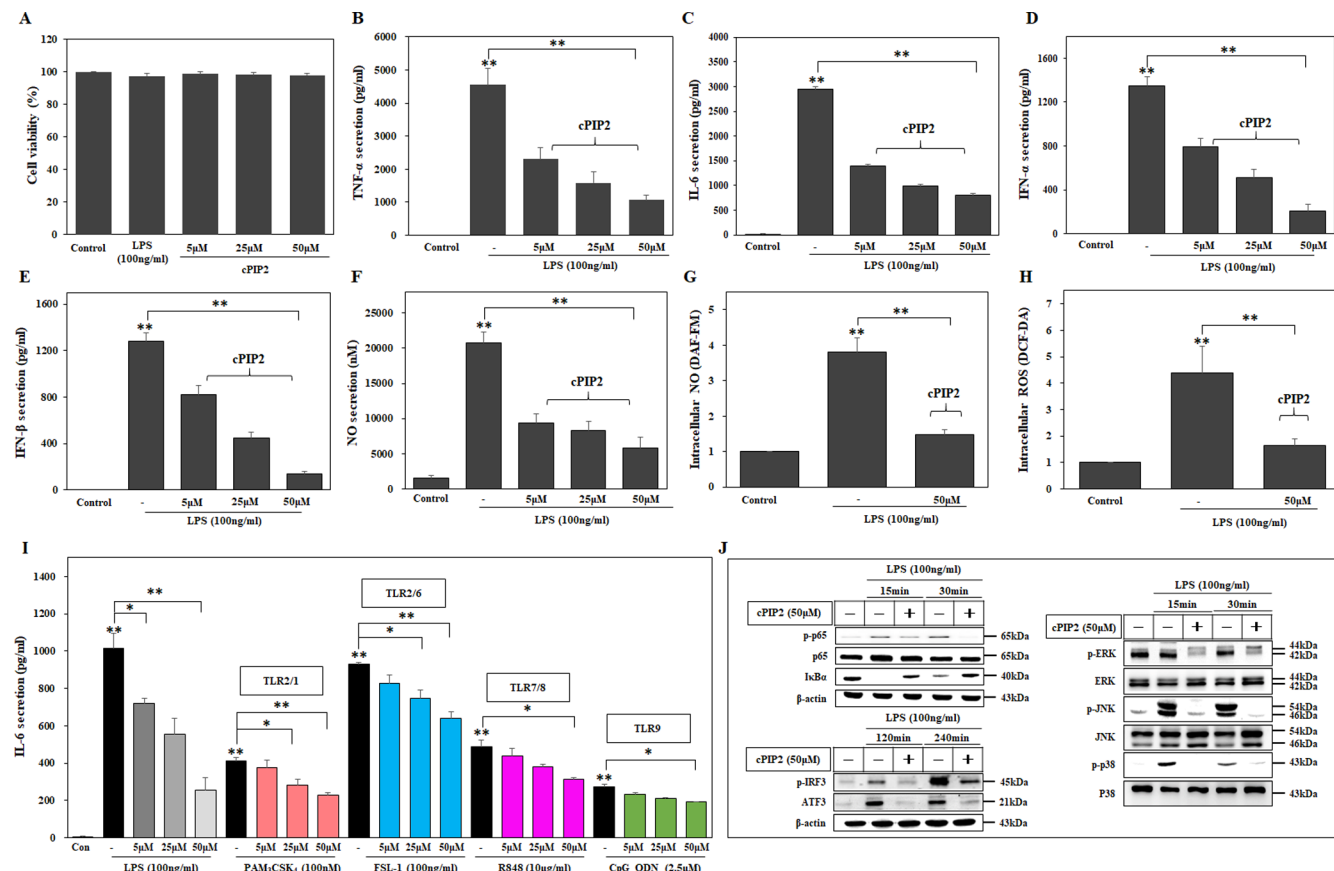


**Figure 7.** Cyclic PIP2 (cPIP2) inhibits proinflammatory cytokine secretion, reduces oxidative stress, and hinders MAPK expression in macrophages. (A) Cell viability was measured by a microplate reader using an MTT assay, and cPIP2 was found to be nontoxic. The secretion levels of (B) TNF- $\alpha$ , (C) IL-6, (D) IFN- $\beta$ , and (E) IFN- $\alpha$  were assessed by ELISA. (F) NO secretion was evaluated using the NO secretion kit. (G) The cytosolic secretion of NO was measured by FACS with DAF-DA staining, and (H) the generation of ROS was measured in the cytosol by FACS using DCF-DA staining. (I) Human monocytic cell (THP-1)-derived macrophages were treated with cPIP2 and challenged with multiple TLR ligands [TLR2/1 ( $\text{PAM}_3\text{CSK}_4$ ), TLR2/6 (FSL-1), TLR9 (CpG-ODN), or TLR7/8 (R848)] to monitor the inhibitory effect of the peptide. cPIP2 significantly hindered TLR4 but other TLRs inadequately. (J) NF- $\kappa$ B activation and the degradation of I $\kappa$ B $\alpha$ , as well as the expression level of MAPKs, were evaluated by western blotting of whole protein extracts. Inactive MAPKs were used as controls, and  $\beta$ -actin was used as a loading control. All data shown are the results of independently conducted experiments ( $n = 4$ ) performed in duplicate; the mean  $\pm$  SEM values of the independent experiments were calculated and used in the two-tailed paired Student's  $t$ -test (\* $P < 0.05$ , \*\* $P < 0.01$ ).

TLR4(TLR4/MD2) complex was deciphered with respect to time. For patch A of the TLR4, we found that Trp8 of PIP2 established a C-H- $\pi$  (arene) bond with Val108, which was further strengthened by the electrostatic contact between Asp155 and the nitrogen atom in the indole group of Trp8. Trajectory analysis suggested that these interactions are quite stable and retained throughout the MD run. In addition, Lys10 established salt bridges with Asp155 and Asp183 after 25 ns of the MD. We found that C-terminal residues of PIP2, which were not in contact with TLR4, established strong hydrogen-bond interactions after 20 ns (Figure 6A). As discussed above, a similar tendency was exhibited by the PIP2-TLR4 system. This consistency suggested that the C-terminus residues, especially the carboxylic group of Val12 and the backbone oxygen of Leu11, were crucial for the stability of PIP2-TLR4 interactions in both dimeric and tetrameric forms [PIP2-TLR4, PIP2-TLR4(TLR4/MD2)] (Figure 6B). The C-terminus motions, based on 500 structural frames extracted from the MD trajectory, have been compiled into 3D (Supporting Movie part 7).

#### Cyclic PIP2 Constrains TLR-Induced Inflammatory Response in Macrophages.

The TLR4-inhibitory potential of cPIP2 was compared in the same cells (macrophages) that were used in the PIP2 analysis. The cytotoxicity of 5, 25, and 50  $\mu$ M cPIP2 was tested in RAW264.7 cells and was found to be nontoxic (Figure 7A). Subsequently, the TLR4-inhibitory effect of cPIP2 was evaluated by monitoring the level of released proinflammatory cytokines in RAW264.7 cells. ELISA showed that the secretion of both the TNF- $\alpha$  and IL-6 was significantly suppressed in a dose-dependent manner (Figure 7B,C). In addition, a significant reduction was noted in type 1 IFNs (IFN- $\alpha$  and IFN- $\beta$ ) in the LPS-stimulated cPIP2-treated cells (Figure 7D,E). The inhibitory effect of cPIP2 on the oxidative stress markers (i.e., NO and ROS) was investigated further. In line with the results of PIP2, the extracellular secretion of NO and the intracellular generation of NO and ROS were significantly inhibited by cPIP2 (Figure 7F–H). Furthermore, the effect of cPIP2 on TLR4 and other TLRs was also investigated through the evaluation of IL-6 secretion in THP-1 cells. The cells were treated with different concentrations of cPIP2 in the presence of different TLR ligands separately [LPS (TLR4),  $\text{PAM}_3\text{CSK}_4$  (TLR1/2), FSL-1 (TLR2/6), resiquimod/R848 (TLR7/8), or CpG-ODN (TLR9)]. We found that cPIP2 showed a significant inhibitory

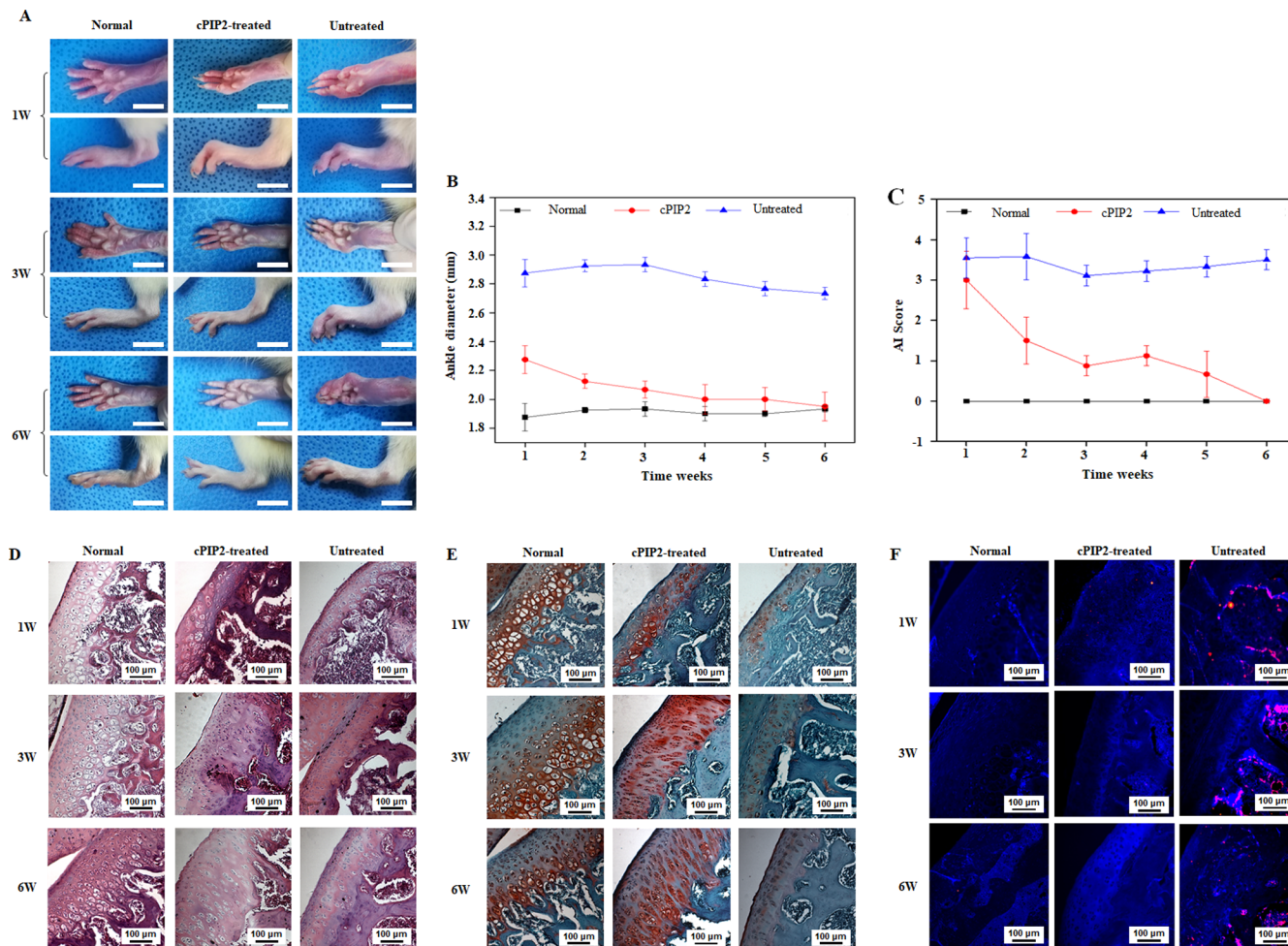


**Figure 8.** cPIP2 alleviates inflammation in the RA rat model. (A) Visual monitoring of the paws of normal (left column), cPIP2-treated (1 nmol/g of rat's weight) (middle column), and untreated RA rats at 1–6 weeks (scale bar = 10 mm). (B) Ankle diameter and (C) articular index scoring of the rats at 1–6 weeks. (D) Hematoxylin and eosin (H&E) staining of the normal, cPIP2-treated, and untreated rats at 1–6 weeks (magnification  $\times 200$ ). (E) Safranin-O (SO) staining images of RA rats after intra-articular injection of cPIP2 at 1–6 weeks (magnification  $\times 200$ ). (F) TNF- $\alpha$  staining of the RA rats after intra-articular injection of cPIP2 at 1–6 weeks (magnification  $\times 200$ ).

effect on TLR4-mediated IL-6 secretion and slightly hindered other TLRs at 50  $\mu$ M (Figure 7I). Moreover, the LPS-induced activation of MAPKs was assessed through western blot analysis in THP-1 cells. The data showed that cPIP2 successfully hindered the activation of NF- $\kappa$ B (phosphorylation of p65 and degradation of I $\kappa$ B $\alpha$ ) and inhibited the phosphorylation level of MAPKs, including ERK, JNK, and p38, compared with the observed expression level following LPS treatment. cPIP2 also inhibited the LPS-induced activation of ATF3 and the phosphorylation of IRF3 (Figure 7J). Collectively, these data suggested that cPIP2 not only maintained the inhibitory characteristics reported for PIP2 but also improved the efficiency of the peptide by reducing the inhibitory concentration ( $IC_{50}$ ) from 40 to 25  $\mu$ M.

#### Cyclic PIP2 Alleviates the TLR4-Mediated Inflammatory Response in Rheumatoid Arthritis (RA) Rat Model

After confirming the inhibitory activity of cPIP2 on LPS-induced inflammatory response in vitro, we further investigated the effect of cPIP2 in vivo using an RA rat model. The rats were separated into three groups ( $n = 3$ ): normal, RA, and cPIP2-treated. RA rats were injected with cPIP2 at a concentration of 1 nmol/g of rat's weight into the articular knee joint for 6 weeks, and the animals were sacrificed at their

selected post-implantation time points (1, 3, and 6 weeks) to assess the therapeutic effects of cPIP2 on RA. First, the effect of cPIP2 on RA rats was evaluated via the visual monitoring of the paws, the measurement of the ankle diameter, and the articular index measurements for 6 weeks. Untreated RA rats showed swollen joints, stiff tarsals, and severe edema and erythema compared to the wild type, during the six weeks of the experimental procedure. However, cPIP2-treated rats showed a substantial reduction in ankle's swelling and edema after two weeks of treatment and regained almost normal feet physiology at 5 to 6 weeks (Figure 8A). Furthermore, ankle diameters and articular index (AI) scores of RA rats were monitored during the 6 weeks of treatment (Figure 8B,C). While the ankle diameters and mean AI scores for untreated RA rats were noticeably high, cPIP2-treated rats significantly decreased both parameters over the time. Further, the extent of inflammation and cartilage degradation during RA pathogenesis was evaluated using hematoxylin and eosin (H&E) staining, safranin-O (SO) staining, and TNF- $\alpha$  staining (Figure 8D–F). The cartilage tissues of the untreated RA rats were compared with those of the normal and cPIP2-injected rats to assess inflammatory cells and articular cartilage destruction. The untreated RA animals did not show any considerable

histological changes in the H&E staining at any time point, while cPIP2-injected RA rats showed a noticeable increase in the cartilage thickness, the presence of few osteocytes after the first week, and evident staining of numerous osteocytes within lacunae after 4 and 6 weeks of cPIP2 treatment (Figure 8D). In SO staining, noticeable positive staining with SO was observed in the sections of synovial tissues from cPIP2-injected rats after 1 week of treatment as compared to the untreated group. The rounded mature chondrocytes were surrounded by glycosaminoglycan (GAG; deep red) deposition, and a noticeable regeneration of GAGs was observed at the border between the cartilage and the bone at 3 weeks (Figure 8E). The stained area was further increased after 6 weeks. These results show that the treatment of RA rats with cPIP2 successfully helped the regeneration of cartilage tissues *in vivo* and alleviated the inflammatory state commonly observed during RA. Furthermore, the immunohistochemical analysis was performed to examine TNF- $\alpha$  expression in synovial tissues obtained from the three different experimental groups (Figure 8F). The synovial tissues of normal rats did not show TNF- $\alpha$  expression, whereas the tissue samples of RA group showed abundant TNF- $\alpha$  expression. Following the injection of cPIP2, the expression level of TNF- $\alpha$  was significantly decreased during first week of treatment. Taken together, these findings support the protective effect of cPIP2 on the RA rat model and suggest that the peptide might be a strong candidate for the development of new peptide-based therapeutics for arthritis and other inflammatory diseases.

## ■ DISCUSSION

TLR4 is a crucial therapeutic target that owes its importance to the strong association it presents with the onset of multiple diseases and to the potency with which it activates an excessive secretion of inflammatory cytokines.<sup>2,11</sup> For these reasons, the development of a novel TLR4 antagonist is a perpetually active field and, so far, includes a variety of proteins, small peptides, chemicals, and antibodies; some of these are in successful clinical trials.<sup>10,11</sup> To inhibit TLR4, a peptide library designed through the PD system was screened for its TLR4 binding and specificity. The peptide, designated as PIP2, was originally selected from the PD library by using hTLR4. PIP2 is a predominantly hydrophobic dodecapeptide ( $\text{NH}_2\text{-LGVFSSWWIKLV-COOH}$ ; sequences provided in Figure 5C with a slightly polar nature owing to two serine and one lysine). To examine the homogeneity/heterogeneity of the peptide in solutions, size-exclusion chromatography (SEC) was conducted. We observed that PIP2 and its structurally constrained derivative, cPIP2, appeared as single peaks, corresponding to their relative retention volume. B12 was used as a reference in this study (Supporting Figure 3). Our empirical results favored the antagonistic effect of the peptide on TLR4 signaling. For example, PIP2 significantly inhibited the LPS-induced inflammatory response, hindering the proinflammatory cytokines and type I IFN secretion, lowering the expression level of MAPKs and reducing the production of oxidative stress markers in different cell lines (Figures 2 and 3). It also successfully hindered the TLR4-mediated inflammation observed *in vivo* following 2 h challenge with LPS (Figure 4).

Furthermore, our *in silico* analysis proposed that PIP2 could block TLR4 signaling by two different possible mechanisms. Due to its hydrophobic nature, we observed that PIP2 preferred to bind MD2 in a TLR4/MD2 complex. This tendency was also observed in a TLR4/MD2 tetrameric

complex. As TLR4 requires MD2, a co-receptor, and an LPS-binding pocket,<sup>36,38</sup> we suggested that blocking the entry of LPS into MD2 could be one of the TLR4-antagonizing mechanisms of PIP2.<sup>24</sup> As PIP2 was initially selected through PD using the ECD of hTLR4, PIP2 was also docked with TLR4 in the absence of MD2. As discussed above, PIP2 clustered at four different positions on the ectodomain of TLR4 (Supporting Figure 2). Previous studies have confirmed that during TLR4 signaling, MD2 interacts with ECD and establishes electrostatic contacts with patches A and B of the TLR4 in mice and humans.<sup>36,39</sup> The comparative structural analysis indicated that the residues in these patches were conserved and were crucial for the TLR4–MD2 interaction. Interestingly, we found that PIP2 could bind to these residues and establish similar contacts. PIP2 specifically recognizes Val108 and Asp155 and stabilizes itself through C-terminal electrostatic interactions with patch B of TLR4. The positively charged arginine in patch B, reported to be crucial for MD2 interaction, was supposedly masked by PIP2. Conclusively, our model suggested that in addition to MD2, which is actively targeted to block TLR4 signaling, blocking TLR4–MD2 interaction can also serve a purpose.

The biological complexity of an organism is indicated by the size of the protein–protein interaction (PPI) interactome.<sup>40</sup> Approximately, half of the druggable human proteins (total ~3000–5000) are expected to be related to the disease state.<sup>41</sup> The role of PPI in understanding biological processes is indispensable. This makes PPI an attractive target for the development of new PPI-modulating entities.<sup>42</sup> The property of ‘druggability’ has been of crucial concern in the search for a potent modulator of deregulated PPIs. The majority of the reported small organic molecules, following Lipinski’s rule of five,<sup>43</sup> modulated PPIs by binding with specific cavities in the target protein. These specific ligand-binding cavities and their success in PPI modulation define the druggability of proteins. Despite the considerable progress that has been made to target PPIs with small molecules, disrupting the PPI interface with small molecules remains an uphill task.<sup>44</sup> Owing to the complex nature of the proteins, the lack of the well-defined pockets, widely distributed and shallow surfaces, and flat protein–protein interfaces, researchers consider such PPIs hard to target with traditional small-molecule-based methods.

Peptide-based therapeutics have overcome the effects of undruggable proteins in challenging PPIs, owing to their protein nature and similar binding mode. The development of peptide or peptidelike drugs is the key method to expand the “druggable genome” by specifically targeting the PPI interface that is less suitable for small organic molecule-based therapies.<sup>45</sup> Peptide drugs offer lower toxicity and enhanced target selectivity compared with small molecules. Notwithstanding their promising efficacy as therapeutics, developing peptide-based drugs is challenging because of their low stability against host proteolytic enzymes that result in shortened *in vivo* activity and low bioavailability. However, it was demonstrated that peptibodies that combine peptides with antibody technology are sufficient to overcome these problems, and the future of peptide drugs is very bright.<sup>46–48</sup>

Peptide stapling, among the other utilized strategies, is used widely to constrain short peptides in an  $\alpha$ -helical conformation. During stapling, the side chains of two amino acids are covalently linked through the lactam bridge (as shown in this study) to form macrocyclic peptides. The lactam link strategy has been widely investigated to enhance the potency of

therapeutic peptides. The Rosenblatt group<sup>49</sup> introduced a lactam link between lysine and aspartic acid (*i* and *i* + 4 positions, respectively) to stabilize the parathyroid-hormone-related protein (PTHrP) analogue; this was subsequently used by other groups to stabilize estrogen-binding coactivator peptides.<sup>50</sup> Chemical crosslinking was also used to link unnatural helix-favoring amino acids that resulted in a potent HIV-1 gp41 inhibitor ( $IC_{50} = 35 \mu\text{M}$ ,  $K_d = 1.2 \mu\text{M}$ ). Using the same lactam linkage strategy (i.e., *i* and *i* + 4 linkage), Fairlie and colleagues reported that constrained peptides were not only superior to the linear analogues but surpassed them.<sup>51</sup>

We implemented a protein design technique to stabilize the proposed helical structure of PIP2 by linking Asp6 and Lysine10 through a lactam bridge (Figure 5C). Structural dynamics suggested that the lactam link stabilized the helical structure and limited the free moment of the N- and C-terminals in cPIP2, compared with that in its linear analogue, PIP2 (Supporting Movie parts 1 and 2). In addition, the backbone and whole protein RMSD of cPIP2 were tremendously stabilized compared with PIP2 (Figure 5C). To ensure that the suggested constrained peptide retained and enhanced its TLR4 inhibitor efficacy, cPIP2 was tested in vitro. We found that cPIP2 not only retained the TLR4-inhibitory effect but also significantly reduced its inhibitory concentration (PIP2  $IC_{50} = 40 \mu\text{M}$ , cPIP2  $IC_{50} = 25 \mu\text{M}$ ) (Figure 7).

RA is a multifactorial autoimmune disease mainly characterized by an erosive inflammation of the articular cartilage, leading to a tumorlike expansion of the synovium and progressive destruction of the adjacent articular cartilage. Although the exact causes of RA remain unknown, the immunological dysregulation observed during the disease has been shown to be involved in driving the inflammation and the synovial cell proliferation.<sup>52,53</sup> To date, numerous studies have examined the involvement of TLR4 in the onset/progression of arthritic diseases to facilitate the discovery of new therapeutic agents.<sup>9,54,55</sup> Accordingly, cPIP2 successfully displayed a protective effect *in vivo* using an RA rat model. The peptide significantly reduced inflammation and helped the regeneration of cartilage tissues (Figure 8).

## CONCLUSIONS

Our study suggests that PIP2, specifically cPIP2, is a promising inhibitor of TLR4 signaling that can successfully alleviate the inflammation observed during RA and, therefore, can act as a lead candidate for the development of TLR4-specific therapeutics to treat auto-inflammatory diseases and related complications.

## EXPERIMENTAL SECTION

**Initial Construction of the Peptide Phage Display Library and TLR4-Based Screening.** The PD peptide library was constructed and screened as previously described.<sup>24</sup> A peptide (12-mer) library was constructed using forward primer 5'-GCC CAG CCG GCC ATG GCC (NNK)<sub>12</sub> TCG AGT GGT GGA GGC GGT TCA G-3' and reverse primer 5'-GCC AGC ATT GAC AGG AGG TTG AG-3'. The randomization codon (NNK; where *N* = A/C/G/T and K = T/G) was employed to cover all potential combinations of amino acids and to evade two stop codons (TAA and TGA). The DNA product was cloned into the pHEN2 phagemid and transfected into electrocompetent DH10B (*E. coli*) cells. Following that, the library was successfully transformed into XL1-Blue (*E. coli*) cells and then amplified. Later, M13K07ΔpIII (hyperphage; PROGEN Biotechnik GmbH, Heidelberg, Germany) was added to the culture (at a final concentration of  $1 \times 10^{12}$  PFU/mL). Following a 30 min

incubation at 37 °C, the cell pellets were collected by centrifugation (3300g, 10 min, 4 °C) and suspended in 30 mL of fresh 2 × YT medium (100 µg/mL ampicillin and 25 µg/mL kanamycin). The cells were incubated overnight at 30 °C. The phage particles were recovered, as described above.

The biopanning procedure was also performed as described previously.<sup>24</sup> Recombinant hTLR4 protein (2.5 µg/mL) was coated into Nunc MaxiSorp 96-well plates (Thermo Fisher Scientific Inc., Waltham, MA) and incubated overnight at 4 °C. The following day, the plate was blocked with 5% skim milk in phosphate-buffered saline (PBS) at room temperature, and the wells were exposed to the phage library. The bound phages were then eluted, recovered, and used for phage titration before the next round of library screening. The phage titer was calculated by colony-forming units (cfu) in XL1-Blue cells on agar plates containing ampicillin (10 µg/mL). The phages were later amplified and purified to be used for the subsequent rounds of panning. In each round (total six rounds), the input and output ratio was calculated to estimate the enrichment efficiency. The selection and isolation of the transfected clones were performed after the sixth round of biopanning through phage-ELISA, as previously described in detail.<sup>24</sup>

### DNA Sequencing and Synthesis of Selected Peptides.

Phages that were selected through phage-ELISA were prepared for the isolation of DNA using the Miniprep kit (GeneAll Biotechnology, Seoul, Korea). Later, the isolated DNA was sequenced by Macrogen, Inc. (Seoul, Korea) using the following primer: 5'-TTG TGA GCG GAT AAC AAT TTC-3'. Then, using BioEdit software,<sup>25</sup> all selected DNA sequences were translated into amino acid and aligned to assess variation.

All peptides tested in the present study were synthesized by Peptron Inc. (Daejeon, Korea) at a purity of at least 95%, as determined by reversed-phase high-performance liquid chromatography (HPLC; Shimadzu Prominence). The Shiseido Capcell pak C18 column (4.6 × 50 mm) was used with 10–60% acetonitrile (ACN) gradient in 0.1% trifluoroacetic acid (TFA)–water, at a flow rate of 1 mL/min, and peaks were detected at 220 nm. The molecular masses of all of the synthesized peptides were determined using Shimadzu LCMS-2020. The analytical data related to peptide (PIP2 and cPIP2) synthesis and purity have been provided in Supporting Data (RP-HPLC analysis for the peptides).

**Cell Culture and Treatment.** HEK-Blue hTLR4 cells (InvivoGen, San Diego, CA) were cultured in Dulbecco's modified Eagle's medium (DMEM; Thermo Fisher Scientific Inc.) supplemented with 10% fetal bovine serum (FBS) (Thermo Fisher Scientific Inc.), 1% penicillin/streptomycin antibiotic mixture, and 0.2% Normocin (InvivoGen). Murine macrophages (RAW264.7 cells) (ATCC, Manassas, VA) were cultured in low-glucose DMEM (Thermo Fisher Scientific Inc.) supplemented with 1% penicillin/streptomycin antibiotic mixture and 10% FBS (Thermo Fisher Scientific, Inc.). hPBMCs, used for western blotting analysis, were purchased from PromoCell (Heidelberg, Germany) and cultured in RPMI 1640 medium supplemented with 10% FBS, 1% penicillin/streptomycin (Thermo Fisher Scientific Inc.), and 1% L-glutamine (Gibco, Grand Island, NY). hPBMCs, used for the evaluation of cytokine secretion, were purchased from Lonza Inc. (Allendale, NJ) and cultured in RPMI 1640 supplemented with 2.05 mM L-glutamine, 1% penicillin/streptomycin, and 10% FBS (Thermo Fisher Scientific, Inc.). mBMDM were cultured in DMEM supplemented with 1% penicillin/streptomycin and 10% FBS (Thermo Fisher Scientific, Inc.). THP-1 cells (kindly gifted by Dr. Chang-Hee Suh, Ajou University, Medical Center, Suwon, Korea) were cultured in RPMI 1640 medium supplemented with 1% penicillin/streptomycin and 10% FBS (Thermo Fisher Scientific, Inc.) and differentiated into macrophages using 80 nM phorbol 12-myristate 13-acetate (PMA; Sigma-Aldrich Co., St. Louis, MO) for 24 h. All cells were incubated in a humidified atmosphere of 5% CO<sub>2</sub> at 37 °C, and all media were changed after 1 night of incubation. Cell treatment was performed with different TLR ligands. LPS (*Escherichia coli* 0111:B4) was purchased from Sigma-Aldrich Co., St. Louis, MO and PAM<sub>2</sub>CSK<sub>4</sub>,

FSL-1, Poly(I:C), R848, and CpG-ODN were all purchased from InvivoGen, San Diego, CA.

**SEAP Activity Assay.** HEK-Blue hTLR4 cells were seeded in 96-well plates at a density of  $2 \times 10^4$  cells/well and incubated for 2 days. The supernatant was removed, and the cells were treated with different concentrations of PIP2 (20, 40, or 80  $\mu\text{M}$ ) in HEK-Blue detection medium (InvivoGen, San Diego, CA) for 1 h, followed by LPS (100 ng/mL) treatment for 24 h. The culture supernatants were collected and placed in a new 96-well plate, and the SEAP activity was assessed through the measurement of the absorbance at 630 nm with a VersaMax microplate reader (Molecular Devices Inc., Sunnyvale, CA).

**Cell Viability Assay.** This parameter was measured colorimetrically using 1-(4,5-dimethylthiazol-2-yl)-3,5-diphenylformazan (MTT) solution (Sigma-Aldrich Co.) diluted in PBS. RAW264.7 cells were seeded at a density of  $2 \times 10^5$  cells/well and treated with different concentrations of the peptides for 24 h. The following day, the medium was removed and replaced by the diluted MTT solution (final concentration, 500  $\mu\text{g}/\text{mL}$ ) (100  $\mu\text{L}/\text{well}$ ). The cells were incubated for 3 h at 37 °C, after which the MTT solution was removed and a dimethyl sulfoxide solution (100  $\mu\text{L}/\text{well}$ ; Sigma-Aldrich Co.) was added. After 30 min, the absorbance at 540 nm was measured spectrophotometrically (Molecular Devices Inc.).

**Protein Expression and Western Blotting.** Whole-protein extraction was performed using M-PER mammalian protein extraction reagents (Thermo Fisher Scientific, Inc.) in accordance with the manufacturer's instructions. Briefly, a mixture of the whole-protein extraction solution (M-PER; Thermo Fisher Scientific Inc.) with protease and phosphatase inhibitor cocktail (Thermo Fisher Scientific Inc.) was added to the cell pellets for 10 min and kept on ice. The chilled cells were then centrifuged at 16 000g for 10 min. The lysate was collected, and the concentration of proteins was measured using the BCA kit (Sigma-Aldrich Co. LLC) in accordance with the manufacturer's instructions. Equal amounts of the protein extracts were loaded into SDS-polyacrylamide gels and transferred to a Hybond-ECL nitrocellulose membrane (Amersham Pharmacia Biotech, Inc., Piscataway, NJ). The membranes were blocked with 0.05% nonfat dried milk in deionized water for 1 h and incubated by immunoblotting with specific primary antibodies (diluted at the ratio of 1:500–1000) against p-p65, p-JNK, p-IRF3, ERK, and p38 (Cell Signaling Technology Inc., Danvers, MA); p-ERK, p-p38, I $\kappa$ B $\alpha$ , JNK, ATF3, COX2,  $\beta$ -actin (Santa Cruz Biotechnology Inc., Santa Cruz, CA), and iNOS (BD Biosciences) were incubated overnight at 4 °C with gentle shaking. On the next day, the membranes were rigorously washed with phosphate-buffered saline containing 0.05% Tween 20 (PBST) and were incubated with anti-mouse/rabbit peroxidase-conjugated immunoglobulin G antibody (Thermo Fisher Scientific Inc.), diluted at the ratio of 1:1000, for 2 h. The proteins were detected using the SuperSignal West Pico ECL solution (Thermo Fisher Scientific Inc.) and visualized using a Fusion solo S system (Vilber Lourmat, France).

**TNF- $\alpha$ , IL-6, IFN- $\beta$ , and IFN- $\alpha$  Secretion.** RAW264.7, mBMDM, THP-1, and hPBMCs cells were seeded in a 96-well plate (BD Biosciences) at a density of  $2 \times 10^5$  cells/well and grown overnight. After 24 h of treatment, the IFN- $\beta$  level was measured by the LEGEND MAX mouse IFN- $\beta$  precoated ELISA kit (BioLegend, San Diego, CA), the IFN- $\alpha$  level was evaluated by the mouse IFN- $\alpha$  platinum precoated ELISA kit (eBioscience, San Diego, CA), and IL-6 secretion was assessed by Mouse/Human IL-6 ELISA MAX Deluxe (BioLegend) or Mouse IL-6 Platinum ELISA (eBioscience, San Diego, CA). TNF- $\alpha$  production was measured by the Mouse TNF  $\alpha$  ELISA Ready-SET-Go kit (eBioscience, San Diego, CA) or Human TNF  $\alpha$  ELISA MAX Deluxe (BioLegend, San Diego, CA). The IL-12/IL-23p40 secretion level was assessed using mouse IL-12/IL-23p40 ELISA MAX Deluxe (BioLegend, San Diego, CA). All experiments were conducted in accordance with the manufacturer's instructions. The plates were read on a microplate spectrophotometer system (Molecular Devices Inc.) at the specified absorbance, and all data were analyzed against a standard curve using SoftMax Pro 5.3 software (Molecular Devices Inc.).

**Cytosolic NO and ROS Measurement Using DAF-FM and DCF-DA Staining.** RAW264.7 cells were seeded at a density of  $1 \times 10^6$  in 6 cm dishes (SPL Life Sciences, Pochun, Korea), incubated overnight, and treated as indicated. The intracellular production of NO and ROS was measured using DAF-FM and DCF-DA dyes (Thermo Fisher Scientific, Inc.), respectively, as described previously.<sup>56</sup> The intensity of fluorescence detected in cells was measured using a FACS Aria III instrument with Diva software (BD Biosciences).

**NO Secretion Analysis.** RAW264.7 and mBMDM cells were seeded at a density of  $2 \times 10^5$  cells/well, grown overnight in 96-well plates (BD Biosciences), and treated as indicated. The secretion level of NO was measured using a nitric oxide detection kit (iNtRON Biotechnology, Gyeonggi, Korea), in accordance with the manufacturer's instructions. The absorbance was measured at 540 nm using a microplate reader spectrophotometer (Molecular Devices Inc.). The data were analyzed against a standard curve using SoftMax Pro 5.3 software (Molecular Devices Inc.).

**Confocal Microscopy.** For the evaluation of p-p65, RAW264.7 cells, grown overnight at a density of  $2 \times 10^5$  cells/well in 24-well plates, were treated with PIP2 (80  $\mu\text{M}$ ) for 1 h and then followed by 30 min treatment with LPS (100 ng/mL). In the case of FITC-PIP2 (Peptron, Inc.), the cells were pretreated with 40  $\mu\text{M}$  FITC-conjugated peptide for 1 h, followed by LPS treatment (100 ng/mL) for 30 min. Subsequently, the cells were fixed with 3.7% formaldehyde solution (Sigma-Aldrich Co.) for 5 min and permeabilized by 0.2% Triton X-100 solution (AMRESCO, Solon, OH) for 5 min. The cells were then washed three times with PBS and blocked with 5% BSA solution (Thermo Fisher Scientific, Inc.) for 30 min. The blocked cells were incubated with primary antibodies against p-p65 (Cell Signaling Technology, 1:1000) or TLR4 (Abcam, Cambridge, UK, 1:1000) for 2 h, followed by three washes with PBS. Next, the cells were incubated with Alexa Fluor 408 and/or 488 secondary antibodies (Invitrogen) for 1 h, washed with PBS, and treated with Hoechst 33258 solution to stain the nuclei (5  $\mu\text{M}$ ; Sigma-Aldrich Co.) for 15 min. The fluorescence intensities were measured using confocal microscopy (LSM-700, Carl Zeiss Microscopy GmbH), and the images were analyzed using Zen 2009 software.

**LPS-Induced *In Vivo* Cytokine Evaluation.** Eight week old C57BL/6 mice (20–25 g,  $n = 5$ ) were obtained from Orient Bio, Inc. (Seoul, Korea). The mice were injected i.p. with PIP2 (70 nmol/g of body weight) for 1 h before being challenged with LPS (5  $\mu\text{g}/\text{g}$  of animal weight) for 2 h. The control group was also injected with an equivalent volume of PBS. The blood plasma samples were collected and kept frozen to be used for the evaluation of proinflammatory cytokine secretion. TNF- $\alpha$  (dilution 1:100), IL-12p40 (1:50) and IL-6 (1:100) were measured using ELISA kits (BioLegend, San Diego, CA). All animal experiments were approved by the Institutional Animal Care and Use Committee (approval number: KHNMC AP 2016-006).

**Preparation and Treatment of the RA Animal Model.** The RA state was induced in the animal model following the administration of 250  $\mu\text{L}$  of the mixed solution containing 0.5 mg bovine type II collagen and complete Freund's adjuvant (v/v) into the tails of 4 week old male Lewis rats ( $n = 3$  for each experimental group). Three weeks following the injection, evidence of edema and erythema was observed in the ankle joints, knee joints, tarsal area, and feet of the animals.

RA treatment experiments were conducted in accordance with the approved guidelines. The protocols of this study were approved by the Institutional Animal Experiment Committee (Approval No. 2013-0070) of the School of Medicine of Ajou University, Korea. The three experimental groups are as follows: normal, untreated, and cPIP2-treated groups. Rats in the treated group were individually injected at a volume of 100  $\mu\text{l}$  of cPIP2 (suspended in PBS at a final concentration of 1154.4  $\mu\text{g}/\text{mL}$ ) into the articular knee joint of the RA animals. The RA animals were individually sacrificed at each of the selected post-implantation time points (1, 3, or 6 weeks;  $n = 3$ ) to assess the therapeutic effects of the treatments.

**Histological Analysis.** At 1, 3, or 6 weeks following the treatment, the animals were sacrificed, and the articular knee joints were dissected individually ( $n = 3$  for each time point). The collected samples were fixed with 10% formalin (Sigma-Aldrich, St. Louis, MO) for 3 days and decalcified using 6% nitric acid (Sigma-Aldrich) for 2 days. The fixed tissues were treated with 100% ethanol for dehydration and then embedded in paraffin. The fixed samples were sectioned into 8  $\mu\text{m}$  slices. The specimens were later stained with hematoxylin and eosin (H&E), safranin-O (SO), and TNF- $\alpha$  stains. For SO staining, the specimens were deparaffinized and hydrated. Then, slides were washed three times and treated with Mayer's hematoxylin solution (Muto Pure Chemicals, Tokyo, Japan) for 5 min, after which the slides were washed again for 20 min. The stained tissues were developed with a 0.002% fast green solution (Sigma-Aldrich) for 30 s and washed with 1% glacial acetic acid. The slides were placed in a 0.1% SO solution (Sigma-Aldrich) for 6 min and then fixed with mounting medium (Muto Pure Chemicals). For TNF- $\alpha$  staining, the slides were incubated for 10 min at 120–130 °C in 10  $\times 10^{-3}$  M sodium citrate buffer solution composed of anhydrous citric acid (Daejung Chemicals, Shiheung, Korea) and anhydrous trisodium citrate (Yakuri Pure Chemicals, Kyoto, Japan) and then washed with PBS. The slides were blocked in PBS containing 10% BSA for 60 min at 37 °C and subsequently incubated at 4 °C overnight with the primary antibodies (rabbit anti-rat TNF- $\alpha$  (1:100); Novus Biologicals, Littleton, CO). Next, the specimens were treated with the secondary antibodies (goat anti-rabbit Alexa Fluor 594; Invitrogen, Carlsbad, CA) (1:200) for 2 h. The slides were later washed and mounted with the ProLong Gold antifade reagent (Thermo Fisher Scientific Inc.). The TNF- $\alpha$ -positive area was calculated as a percentage of the total cartilage area using ImageJ software (National Institute of Health, Bethesda, MD) from three randomly selected fields for each specimen. The immunofluorescence photos were attained using an Axio Imager A1 (Carl Zeiss Microimaging GmbH, Gottingen, Germany) and evaluated with Axiovision software (Rel. 4.8; Carl Zeiss Microimaging GmbH).

**Measurement of Ankle Diameter in RA Rats and Calculation of the Articular Index Score.** The hind paws of each group (RA, cPIP2-injected, and normal rats) were examined to determine the AI score and ankle diameter every week for 6 weeks. The ankle diameter was measured in three rats using Vernier calipers. AI was blind tested and scored as follows: no edema or erythema (score 0), slight edema and erythema (+1), moderate edema and shackles (+2), edema with limited use of joints and symptoms of enlargement to the metatarsal (+3), and excessive swelling as a serious symptom associated with joint ankyloses and total hind paw (+4). All ankle diameters and AI scores were independently measured three times, and the results were presented as the mean  $\pm$  standard deviation (SD).

**Protein Modeling and Protein–Protein Docking Simulations.** The 3D models of the PIP2 oligopeptide were generated through MOE (2016.08) and I-TASSER online server.<sup>32</sup> The structures showed the same folds, and a TM score<sup>57</sup> >0.5 in I-TASSER was selected and further validated. The overall geometric and stereochemical properties of the final 3D-modeled peptides were examined through Ramachandran plots generated by MOE and PROCHECK.<sup>58</sup> To assess the binding affinity of PIP2 with the human TLR4/MD2 complex, relevant X-ray crystal structures were retrieved from PDB (3FXI). The bound ligands and unbound water molecules were removed from the crystal structure and further inspected for abnormalities using a structural preparation package distributed in MOE. To assess the binding affinity and suggest the most plausible TLR4-antagonizing mechanism of PIP2, the following conditions in which PIP2 could bind to TLR4 were considered: (i) the ectodomain of monomeric TLR4; (ii) the ectodomain of monomeric TLR4 bound to MD2; and (iii) the dimeric ectodomain of TLR4, where one monomer was attached to MD2 and the other monomer was kept vacant. The online protein–protein docking servers ZDOCK<sup>59</sup> and standalone MOE suit were used to predict and assess the interaction mechanism between PIP2 and TLR4, as previously discussed.<sup>60</sup> Briefly, TLRs were kept as receptors and PIP2

was considered as a ligand in each round of docking. Five hundred docking conformations were generated for each target TLR and PIP2, using ZDOCK and MOE, separately. The consistent docking poses were selected on the basis of protein ligand interaction fingerprints (PLIFs) distributed in MOE. The docking clusters with the consistent population (PIP2-TLR interface information) were filtered and further investigated for interfacial analysis. After the initial evaluation of PIP2 as a potent TLR4 antagonist, the peptide cyclization strategy was implemented to stabilize its proposed helical structure and enhance the inhibitory efficacy. The protein design algorithm, implemented in MOE, was used to examine the possible residues that could be mutated or modified to assist the stability of the peptide, as well as enhance its TLR4-binding affinity. Among the suggested modifications, the Ser6/Asp mutation was selected, and a lactam bridge was created between the charged NH<sup>3+</sup> of Lys10 and COO<sup>-</sup> of Asp6 sidechains and named cPIP2. cPIP2 was further investigated for its structural stability, through protein dynamics, and in vitro efficacy (discussed in Results).

**Molecular Dynamics and Structural Stabilization of the Peptides.** The best model of PIP2 selected from I-TASSER and its cyclic form, cPIP2, were subjected to MD simulation under AMBER99SB-ILDNP force field<sup>61</sup> using GROMACS v5.6.2. The systems were solvated under periodic boundary conditions in a cubic box filled with TIP3P water type.<sup>62</sup> Counter ions, Na<sup>+</sup> and Cl<sup>-</sup>, were added to neutralize the systems before equilibration. The neutralized systems were energy-minimized with a tolerance of 100 kJ/mol with no constraints and further subjected to a two-step equilibration. To avoid any conformational change, position restraints were applied to all atoms during the equilibration phases. Each system was simulated for 200 ps under the NVT (number of particles, volume of the system, and temperature of the system remained constant) ensemble, and the protein and solvent were treated as separate groups for temperature coupling in the V-rescale method.<sup>63</sup> In the second round of equilibration, the systems were treated at a constant pressure of 1.0 bar under NPT conditions,<sup>64</sup> applying the constraint to all bonds under the LINCS algorithm.<sup>65</sup> The equilibrated structures were simulated under NPT conditions, without any position restraint for 1  $\mu\text{s}$  (PIP2) and 150 ns (cPIP2), respectively. The coordinates were saved every 2 ps, under constant pressure and temperature (300 K), for the entire production run. Further analyses were implemented to investigate the stability of the peptides and considered reliable for protein–protein docking studies. All figures and illustrations were generated in Pymol, MOE, and Chimera<sup>66</sup> and compiled in PowerPoint. The key interacting residues at the protein–protein interfaces were highlighted and identified in Chimera and MOE.

**Binding Kinetics of PIP2 and cPIP2 Using SPR.** SPR experiments were performed using the ProteOn XPR36 instrument (Bio-Rad Laboratories, Inc.) with a ProteOn GLM sensor chip and Biacore T200 instrument (HyClone Laboratories, Inc.) with a Biacore C1 sensor chip. PBS supplemented with 0.1% Tween 20 (PBST containing 2% DMSO) was used as running buffer and 10 mM HCl or PBST 0.1% for regeneration. hTLR4, hTLR2, and hMD2 (R&D systems) were immobilized by amine coupling onto the surfaces of a GLM sensor chip (Bio-Rad Laboratories, Inc.) or C1 sensor chip (HyClone Laboratories, Inc.). Varying concentrations of the PIP2 and cPIP2 molecules (0, 12.5, 25, 50, 100, and 200  $\mu\text{M}$ ) were injected into the chips to evaluate their binding with the immobilized proteins; running buffer was injected into the empty channel as a reference. The experiments were performed in duplicate using freshly prepared reagents. ProteOn manager software (version 2.0) and Biacore T200 evaluation software (version 3.0) were used to analyze the data. The binding curves were processed for determining the starting injection alignment and baseline. The reference-subtracted sensorgram was fitted globally to the curves describing a homogeneous 1:1 Langmuir bimolecular reaction model. Data from the protein surfaces were grouped to fit the kinetic rate constants ( $k_a$  and  $k_d$ ). The binding constant,  $K_D$ , was calculated from the equation

$$K_D = k_d/k_a$$

**Size-Exclusion Chromatography (SEC).** Size-exclusion chromatography was performed to analyze whether the peptides are homogeneous. The Superdex 30 column (GE Healthcare) was connected to an NGC Quest 10 Plus chromatography system (Bio-Rad) and equilibrated with degassed running buffer (30% (v/v) acetonitrile, 0.1% (v/v) trifluoroacetic acid, pH 7.0). The peptides and vitamin B12 were injected into the column and eluted with the running buffer. The eluted peaks were analyzed using ChromLab software (Bio-Rad). Data analysis was carried using ChromLab software (Bio-Rad Laboratories Inc.).

**Statistical Analysis.** All data presented in this work were obtained from at least three independent experiments. The statistical significance was defined by *P* values of <0.05 or <0.01, using the two-tailed paired Student's *t*-test in SigmaPlot software, version 12.0 (Systat Software Inc., San Jose, CA).

## ■ ASSOCIATED CONTENT

### Supporting Information

The Supporting Information is available free of charge on the ACS Publications website at DOI: [10.1021/acs.jmedchem.9b00061](https://doi.org/10.1021/acs.jmedchem.9b00061).

Table 1, amino acid sequence of the phage display selected peptides; Table 2, secondary structure prediction and homology modeling parameters of PIP2; Figure 1, biophysical interaction of PIP2 with TLR2; Figure 2, comparative binding interface and protein ligand interaction fingerprint (PLIF) analysis of the PIP2-bound TLR4 in the presence and absence of MD2; Figure 3, size-exclusion chromatography analysis of the peptides ([PDF](#))

RP-HPLC analysis for the peptides.

Supporting Movie, the continuous motion of the 3D coordinates of the proteins during molecular dynamics simulations; with relevant information at the beginning of each part inside the movie file ([MP4](#))

4 PDB structures of the complexes used in this study ([PDB](#)) ([PDB](#)) ([PDB](#)) ([PDB](#))

## ■ AUTHOR INFORMATION

### Corresponding Author

\*E-mail: [sangdunchoi@ajou.ac.kr](mailto:sangdunchoi@ajou.ac.kr).

### ORCID

Tae Hyeon Yoo: [0000-0003-1448-3165](http://orcid.org/0000-0003-1448-3165)

Moon Suk Kim: [0000-0002-6689-1825](http://orcid.org/0000-0002-6689-1825)

Sangdun Choi: [0000-0001-5920-7848](http://orcid.org/0000-0001-5920-7848)

### Author Contributions

A.A. and S.C. conceived the project. A.A., X.G., B.L., and T.Y. constructed phage libraries and performed the HTS. A.A., X.G., H.J.S, and E.Y.C. performed the in vitro experiments and analyzed the relevant data. A.A., H.K., and D.J.K. performed the in vivo experiments. M.S. designed cPIP2, performed the in silico experiments, and analyzed the relevant data. A.A. and M.S. wrote the manuscript. S.C. coordinated the project and wrote the manuscript. All authors have given their approval to the final version of the manuscript.

### Notes

The authors declare no competing financial interest.

## ■ ACKNOWLEDGMENTS

This work was supported by the National Research Foundation of Korea (NRF-2019M3A9A8065098) and the Commercializations Promotion Agency for R&D Outcomes funded by the Ministry of Science and ICT (2018K000369).

## ■ ABBREVIATIONS USED

ATF3, activating transcription factor 3; IL-1 $\beta$ , interleukin-1 $\beta$ ; IRF3, interferon regulatory transcription factor 3; MAPK, mitogen-activated protein kinase; MD, molecular dynamics; Myd88, myeloid differentiation primary response gene 88; NF- $\kappa$ B, nuclear factor- $\kappa$ B; SPR, surface plasmon resonance (SPR); TLR, toll-like receptor; TRIF, toll/interleukin-1 receptor (TIR)-domain-containing adapter-inducing interferon- $\beta$

## ■ REFERENCES

- Duffy, L.; O'Reilly, S. C. Toll-like receptors in the pathogenesis of autoimmune diseases: recent and emerging translational developments. *ImmunoTargets Ther.* **2016**, *5*, 69–80.
- Achek, A.; Yesudhas, D.; Choi, S. Toll-like receptors: promising therapeutic targets for inflammatory diseases. *Arch. Pharmacal Res.* **2016**, *39*, 1032–1049.
- Nijland, R.; Hofland, T.; van Strijp, J. A. Recognition of LPS by TLR4: potential for anti-inflammatory therapies. *Mar. Drugs* **2014**, *12*, 4260–4273.
- Akira, S. Pathogen recognition by innate immunity and its signaling. *Proc. Jpn. Acad., Ser. B* **2009**, *85*, 143–156.
- Kawai, T.; Akira, S. The role of pattern-recognition receptors in innate immunity: update on Toll-like receptors. *Nat. Immunol.* **2010**, *11*, 373–384.
- Kawai, T.; Akira, S. Toll-like receptors and their crosstalk with other innate receptors in infection and immunity. *Immunity* **2011**, *34*, 637–650.
- Yang, Y.; Lv, J.; Jiang, S.; Ma, Z.; Wang, D.; Hu, W.; Deng, C.; Fan, C.; Di, S.; Sun, Y.; Yi, W. The emerging role of Toll-like receptor 4 in myocardial inflammation. *Cell Death Dis.* **2016**, *7*, No. e2234.
- Lee, Y. S.; Park, J. S.; Jung, S. M.; Kim, S. D.; Kim, J. H.; Lee, J. Y.; Jung, K. C.; Mamura, M.; Lee, S.; Kim, S. J.; Bae, Y. S.; Park, S. H. Inhibition of lethal inflammatory responses through the targeting of membrane-associated Toll-like receptor 4 signaling complexes with a smad6-derived peptide. *EMBO Mol. Med.* **2015**, *7*, 577–592.
- Pierer, M.; Wagner, U.; Rossol, M.; Ibrahim, S. Toll-like receptor 4 is involved in inflammatory and joint destructive pathways in collagen-induced arthritis in DBA/1J mice. *PLoS One* **2011**, *6*, No. e23539.
- Basith, S.; Manavalan, B.; Lee, G.; Kim, S. G.; Choi, S. Toll-like receptor modulators: a patent review (2006–2010). *Expert Opin. Ther. Pat.* **2011**, *21*, 927–944.
- Patra, M. C.; Choi, S. Recent progress in the development of Toll-like receptor (TLR) antagonists. *Expert Opin. Ther. Pat.* **2016**, *26*, 719–730.
- Matsunaga, N.; Tsuchimori, N.; Matsumoto, T.; Ii, M. TAK-242 (resatorvid), a small-molecule inhibitor of Toll-like receptor (TLR) 4 signaling, binds selectively to TLR4 and interferes with interactions between TLR4 and its adaptor molecules. *Mol. Pharmacol.* **2011**, *79*, 34–41.
- Shirey, K. A.; Lai, W.; Scott, A. J.; Lipsky, M.; Mistry, P.; Pletnevna, L. M.; Karp, C. L.; McAlees, J.; Gioannini, T. L.; Weiss, J.; Chen, W. H.; Ernst, R. K.; Rossignol, D. P.; Gusovsky, F.; Blanco, J. C.; Vogel, S. N. The TLR4 antagonist Eritoran protects mice from lethal influenza infection. *Nature* **2013**, *497*, 498–502.
- Perrin-Cocon, L.; Aublin-Gex, A.; Sestito, S. E.; Shirey, K. A.; Patel, M. C.; Andre, P.; Blanco, J. C.; Vogel, S. N.; Peri, F.; Lotteau, V. TLR4 antagonist FP7 inhibits LPS-induced cytokine production and glycolytic reprogramming in dendritic cells, and protects mice from lethal influenza infection. *Sci. Rep.* **2017**, *7*, No. 40791.
- Cighetti, R.; Ciaramelli, C.; Sestito, S. E.; Zanoni, I.; Kubik, L.; Arda-Freire, A.; Calabrese, V.; Granucci, F.; Jerala, R.; Martin-Santamaria, S.; Jimenez-Barbero, J.; Peri, F. Modulation of CD14 and TLR4.MD-2 activities by a synthetic lipid A mimetic. *ChemBioChem* **2014**, *15*, 250–258.
- Peri, F.; Calabrese, V. Toll-like receptor 4 (TLR4) modulation by synthetic and natural compounds: an update. *J. Med. Chem.* **2014**, *57*, 3612–3622.

- (17) Yamamoto, H.; Oda, M.; Kanno, M.; Tamashiro, S.; Tamura, I.; Yoneda, T.; Yamasaki, N.; Domon, H.; Nakano, M.; Takahashi, H.; Terao, Y.; Kasai, Y.; Imagawa, H. Chemical hybridization of Vizantin and lipid A to generate a novel LPS antagonist. *Chem. Pharm. Bull.* **2016**, *64*, 246–257.
- (18) Cochet, F.; Facchini, F. A.; Zaffaroni, L.; Billod, J. M.; Coelho, H.; Holgado, A.; Braun, H.; Beyaert, R.; Jerala, R.; Jimenez-Barbero, J.; Martin-Santamaria, S.; Peri, F. Novel carboxylate-based glycolipids: TLR4 antagonism, MD-2 binding and self-assembly properties. *Sci. Rep.* **2019**, *9*, No. 919.
- (19) Peri, F.; Piazza, M. Therapeutic targeting of innate immunity with Toll-like receptor 4 (TLR4) antagonists. *Biotechnol. Adv.* **2012**, *30*, 251–260.
- (20) Monnet, E.; Lapeyre, G.; Poelgeest, E. V.; Jacqmin, P.; Graaf, K.; Reijers, J.; Moerland, M.; Burggraaf, J.; Min, C. Evidence of NI-0101 pharmacological activity, an anti-TLR4 antibody, in a randomized phase I dose escalation study in healthy volunteers receiving LPS. *Clin. Pharmacol. Ther.* **2017**, *101*, 200–208.
- (21) Smith, G. P.; Scott, J. K. Libraries of peptides and proteins displayed on filamentous phage. *Methods Enzymol.* **1993**, *217*, 228–257.
- (22) Taylor, J. W. The synthesis and study of side-chain lactam-bridged peptides. *Biopolymers* **2002**, *66*, 49–75.
- (23) Davies, J. S. The cyclization of peptides and depsipeptides. *J. Pept. Sci.* **2003**, *9*, 471–501.
- (24) Park, S.; Shin, H. J.; Shah, M.; Cho, H. Y.; Anwar, M. A.; Ache, A.; Kwon, H. K.; Lee, B.; Yoo, T. H.; Choi, S. TLR4/MD2 specific peptides stalled in vivo LPS-induced immune exacerbation. *Biomaterials* **2017**, *126*, 49–60.
- (25) Hall, T. A. A user-friendly biological sequence alignment editor and analysis program for Windows 95/98/NT. *Nucleic Acids Symposium Series*; Information Retrieval Ltd.: London, 1999; Vol. 41, pp 95–98.
- (26) Fujioka, S.; Niu, J.; Schmidt, C.; Sclabas, G. M.; Peng, B.; Uwagawa, T.; Li, Z.; Evans, D. B.; Abbruzzese, J. L.; Chiao, P. J. NF-kappaB and AP-1 connection: mechanism of NF-kappaB-dependent regulation of AP-1 activity. *Mol. Cell. Biol.* **2004**, *24*, 7806–7819.
- (27) Kim, J. Y.; Park, S. J.; Yun, K. J.; Cho, Y. W.; Park, H. J.; Lee, K. T. *Eur. J. Pharmacol.* **2008**, *584*, 175–184.
- (28) Liu, K.-L.; Chen, H.-W.; Wang, R.-Y.; Lei, Y.-P.; Sheen, L.-Y.; Lii, C.-K. DATS reduces LPS-induced iNOS expression, NO production, oxidative stress, and NF- $\kappa$ B activation in RAW 264.7 macrophages. *J. Agric. Food Chem.* **2006**, *54*, 3472–3478.
- (29) West, A. P.; Brodsky, I. E.; Rahner, C.; Woo, D. K.; Erdjument-Bromage, H.; Tempst, P.; Walsh, M. C.; Choi, Y.; Shadel, G. S.; Ghosh, S. TLR signalling augments macrophage bactericidal activity through mitochondrial ROS. *Nature* **2011**, *472*, 476–480.
- (30) Manček-Keber, M.; Frank-Bertoncelj, M.; Hafner-Bratkovič, I.; Smole, A.; Zorko, M.; Pirher, N.; Hayer, S.; Kralj-Iglič, V.; Rozman, B.; Ilc, N.; et al. Toll-like receptor 4 senses oxidative stress mediated by the oxidation of phospholipids in extracellular vesicles. *Sci. Signal.* **2015**, *8*, No. ra60.
- (31) Drescher, D. G.; Ramakrishnan, N. A.; Drescher, M. J. Surface plasmon resonance (SPR) analysis of binding interactions of proteins in inner-ear sensory epithelia. *Methods Mol. Biol.* **2009**, *493*, 323–343.
- (32) Zhang, Y. I-TASSER server for protein 3D structure prediction. *BMC Bioinf.* **2008**, *9*, No. 40.
- (33) Dietrich, L.; Rathmer, B.; Ewan, K.; Bange, T.; Heinrichs, S.; Dale, T. C.; Schade, D.; Grossmann, T. N. Cell permeable stapled peptide inhibitor of wnt signaling that targets beta-catenin protein-protein interactions. *Cell Chem. Biol.* **2017**, *24*, 958–968.
- (34) Verdine, G. L.; Hilinski, G. J. Stapled Peptides for Intracellular Drug Targets. *Methods in Enzymology*; Academic Press, 2012; Vol. 503, pp 3–33.
- (35) White, A. M.; Craik, D. J. Discovery and optimization of peptide macrocycles. *Expert Opin. Drug Discovery* **2016**, *11*, 1151–1163.
- (36) Kim, H. M.; Park, B. S.; Kim, J. I.; Kim, S. E.; Lee, J.; Oh, S. C.; Enkhbayar, P.; Matsushima, N.; Lee, H.; Yoo, O. J.; Lee, J. O. Crystal structure of the TLR4-MD-2 complex with bound endotoxin antagonist Eritoran. *Cell* **2007**, *130*, 906–917.
- (37) Shah, M.; Anwar, M. A.; Yesudhas, D.; Krishnan, J.; Choi, S. A structural insight into the negative effects of opioids in analgesia by modulating the TLR4 signaling: an in silico approach. *Sci. Rep.* **2016**, *6*, No. 39271.
- (38) Ohnishi, T.; Muroi, M.; Tanamoto, K. MD-2 is necessary for the toll-like receptor 4 protein to undergo glycosylation essential for its translocation to the cell surface. *Clin. Diagn. Lab. Immunol.* **2003**, *10*, 405–410.
- (39) Park, B. S.; Song, D. H.; Kim, H. M.; Choi, B. S.; Lee, H.; Lee, J. O. The structural basis of lipopolysaccharide recognition by the TLR4-MD-2 complex. *Nature* **2009**, *458*, 1191–1195.
- (40) Stumpf, M. P.; Thorne, T.; de Silva, E.; Stewart, R.; An, H. J.; Lappe, M.; Wiuf, C. Estimating the size of the human interactome. *Proc. Natl. Acad. Sci. USA* **2008**, *105*, 6959–6964.
- (41) Hambly, K.; Danzer, J.; Muskal, S.; Debe, D. A. Interrogating the druggable genome with structural informatics. *Mol. Diversity* **2006**, *10*, 273–281.
- (42) Archakov, A. I.; Govorun, V. M.; Dubanov, A. V.; Ivanov, Y. D.; Veselovsky, A. V.; Lewi, P.; Janssen, P. Protein-protein interactions as a target for drugs in proteomics. *Proteomics* **2003**, *3*, 380–391.
- (43) Lipinski, C. A.; Lombardo, F.; Dominy, B. W.; Feeney, P. J. Experimental and computational approaches to estimate solubility and permeability in drug discovery and development settings. *Adv. Drug Delivery Rev.* **2001**, *46*, 3–26.
- (44) Wells, J. A.; McClendon, C. L. Reaching for high-hanging fruit in drug discovery at protein-protein interfaces. *Nature* **2007**, *450*, 1001–1009.
- (45) Hopkins, A. L.; Groom, C. R. The druggable genome. *Nat. Rev. Drug Discovery* **2002**, *1*, 727–730.
- (46) Newland, A.; Caulier, M. T.; Kappers-Klunne, M.; Schipperus, M. R.; Lefrere, F.; Zwaginga, J. J.; Christal, J.; Chen, C. F.; Nichol, J. L. An open-label, unit dose-finding study of AMG 531, a novel thrombopoiesis-stimulating peptibody, in patients with immune thrombocytopenic purpura. *Br. J. Haematol.* **2006**, *135*, 547–553.
- (47) Coxon, A.; Bready, J.; Min, H.; Kaufman, S.; Leal, J.; Yu, D.; Lee, T. A.; Sun, J. R.; Estrada, J.; Bolon, B.; McCabe, J.; Wang, L.; Rex, K.; Caenepeel, S.; Hughes, P.; Cordover, D.; Kim, H.; Han, S. J.; Michaels, M. L.; Hsu, E.; Shimamoto, G.; Cattley, R.; Hurh, E.; Nguyen, L.; Wang, S. X.; Ndifor, A.; Hayward, I. J.; Falcon, B. L.; McDonald, D. M.; Li, L.; Boone, T.; Kendall, R.; Radinsky, R.; Oliner, J. D. Context-dependent role of angiopoietin-1 inhibition in the suppression of angiogenesis and tumor growth: implications for AMG 386, an angiopoietin-1/2-neutralizing peptibody. *Mol. Cancer Ther.* **2010**, *9*, 2641–2651.
- (48) Hsu, H.; Khare, S. D.; Lee, F.; Miner, K.; Hu, Y. L.; Stolina, M.; Hawkins, N.; Chen, Q.; Ho, S. Y.; Min, H.; Xiong, F.; Boone, T.; Zack, D. J. A novel modality of BAFF-specific inhibitor AMG623 peptibody reduces B-cell number and improves outcomes in murine models of autoimmune disease. *Clin. Exp. Rheumatol.* **2012**, *30*, 197–201.
- (49) Chorev, M.; Roubini, E.; McKee, R. L.; Gibbons, S. W.; Goldman, M. E.; Caulfield, M. P.; Rosenblatt, M. Cyclic parathyroid hormone related protein antagonists: lysine 13 to aspartic acid 17 [i to (i + 4)] side chain to side chain lactamization. *Biochemistry* **1991**, *30*, 5968–5974.
- (50) Geistlinger, T. R.; Guy, R. K. Novel selective inhibitors of the interaction of individual nuclear hormone receptors with a mutually shared steroid receptor coactivator 2. *J. Am. Chem. Soc.* **2003**, *125*, 6852–6853.
- (51) Harrison, R. S.; Shepherd, N. E.; Hoang, H. N.; Ruiz-Gomez, G.; Hill, T. A.; Driver, R. W.; Desai, V. S.; Young, P. R.; Abbenante, G.; Fairlie, D. P. Downsizing human, bacterial, and viral proteins to short water-stable alpha helices that maintain biological potency. *Proc. Natl. Acad. Sci. USA* **2010**, *107*, 11686–11691.
- (52) Isaacs, J. D. The changing face of rheumatoid arthritis: sustained remission for all? *Nat. Rev. Immunol.* **2010**, *10*, 605–611.

- (53) Smolen, J. S.; Aletaha, D.; Barton, A.; Burmester, G. R.; Emery, P.; Firestein, G. S.; Kavanaugh, A.; McInnes, I. B.; Solomon, D. H.; Strand, V.; Yamamoto, K. Rheumatoid arthritis. *Nat. Rev. Dis. Primers* **2018**, *4*, 16–23.
- (54) Roelofs, M. F.; Wenink, M. H.; Brentano, F.; Abdollahi-Roodsaz, S.; Oppers-Walgreen, B.; Barrera, P.; van Riel, P. L.; Joosten, L. A.; Kyburz, D.; van den Berg, W. B.; Radstake, T. R. Type I interferons might form the link between Toll-like receptor (TLR) 3/7 and TLR4-mediated synovial inflammation in rheumatoid arthritis (RA). *Ann. Rheum. Dis.* **2009**, *68*, 1486–1493.
- (55) Wang, Y.; Chen, L.; Li, F.; Bao, M.; Zeng, J.; Xiang, J.; Luo, H.; Li, J.; Tang, L. TLR4 rs41426344 increases susceptibility of rheumatoid arthritis (RA) and juvenile idiopathic arthritis (JIA) in a central south Chinese han population. *Pediatr. Rheumatol.* **2017**, *15*, 12–20.
- (56) Shin, H. J.; Kwon, H. K.; Lee, J. H.; Gui, X.; Ache, A.; Kim, J. H.; Choi, S. Doxorubicin-induced necrosis is mediated by poly-(ADP-ribose) polymerase 1 (PARP1) but is independent of p53. *Sci. Rep.* **2015**, *5*, No. 15798.
- (57) Bowie, J. U.; Luthy, R.; Eisenberg, D. A method to identify protein sequences that fold into a known three-dimensional structure. *Science* **1991**, *253*, 164–170.
- (58) Laskowski, R. A.; Rullmann, J. A.; MacArthur, M. W.; Kaptein, R.; Thornton, J. M. AQUA and PROCHECK-NMR: programs for checking the quality of protein structures solved by NMR. *J. Biomol. NMR* **1996**, *8*, 477–486.
- (59) Chen, R.; Li, L.; Weng, Z. ZDOCK: an initial-stage protein-docking algorithm. *Proteins* **2003**, *52*, 80–87.
- (60) Shah, M.; Anwar, M. A.; Park, S.; Jafri, S. S.; Choi, S. In silico mechanistic analysis of IRF3 inactivation and high-risk HPV E6 species-dependent drug response. *Sci. Rep.* **2015**, *5*, No. 13446.
- (61) Lindorff-Larsen, K.; Piana, S.; Palmo, K.; Maragakis, P.; Klepeis, J. L.; Dror, R. O.; Shaw, D. E. Improved side-chain torsion potentials for the Amber ff99SB protein force field. *Proteins* **2010**, *78*, 1950–1958.
- (62) Jorgensen, W. L.; Chandrasekhar, J.; Madura, J. D.; Impey, R. W.; Klein, M. L. Comparison of simple potential functions for simulating liquid water. *J. Chem. Phys.* **1983**, *79*, 926–935.
- (63) Bussi, G.; Donadio, D.; Parrinello, M. Canonical sampling through velocity rescaling. *J. Chem. Phys.* **2007**, *126*, No. 014101.
- (64) Parrinello, M.; Rahman, A. Polymorphic transitions in single crystals: a new molecular dynamics method. *J. Appl. Phys.* **1981**, *52*, 7182–7190.
- (65) Hess, B.; Bekker, H.; Berendsen, H. J.; Fraaije, J. G. LINCS: a linear constraint solver for molecular simulations. *J. Comput. Chem.* **1997**, *18*, 1463–1472.
- (66) Pettersen, E. F.; Goddard, T. D.; Huang, C. C.; Couch, G. S.; Greenblatt, D. M.; Meng, E. C.; Ferrin, T. E. UCSF Chimera—a visualization system for exploratory research and analysis. *J. Comput. Chem.* **2004**, *25*, 1605–1612.